

# An unambiguous AGN and a Balmer break in an Ultraluminous Little Red Dot at $z=4.47$ from Ultradeep UNCOVER and All the Little Things Spectroscopy

IVO LABBE,<sup>1</sup> JENNY E. GREENE,<sup>2</sup> JORRYT MATTHEE,<sup>3</sup> HELENA TREIBER,<sup>2</sup> VASILY KOKOREV,<sup>4</sup> TIM B. MILLER,<sup>5</sup> IVAN KRAMARENKO,<sup>3</sup> DAVID J. SETTON,<sup>2,\*</sup> YILUN MA (马逸伦),<sup>2</sup> ANDY D. GOULDING,<sup>2</sup> RACHEL BEZANSON,<sup>6</sup> ROHAN P. NAIDU,<sup>7,†</sup> CHRISTINA C. WILLIAMS,<sup>8</sup> HAKIM ATEK,<sup>9</sup> GABRIEL BRAMMER,<sup>10</sup> SAM E. CUTLER,<sup>11</sup> IRYNA CHERMERYNSKA,<sup>9</sup> AIDAN P. CLOONAN,<sup>11</sup> PRATIKA DAYAL,<sup>12</sup> ANNA DE GRAAFF,<sup>13</sup> YOSHINOBU FUDAMOTO,<sup>14</sup> SEIJI FUJIMOTO,<sup>4,‡</sup> LUKAS J. FURTAK,<sup>15</sup> KARL GLAZEBROOK,<sup>16</sup> KASPER E. HEINTZ,<sup>17,18,19</sup> JOEL LEJA,<sup>20,21,22</sup> DANILO MARCHESINI,<sup>23</sup> THEMIYA NANAYAKKARA,<sup>16</sup> ERICA J. NELSON,<sup>24</sup> PASCAL A. OESCH,<sup>19,10</sup> RICHARD PAN,<sup>25</sup> SEDONA H. PRICE,<sup>6</sup> IRENE SHIVAEI,<sup>26</sup> DAVID SOBRAL,<sup>27,28</sup> KATHERINE A. SUESS,<sup>29,§</sup> PIETER VAN DOKKUM,<sup>30</sup> BINGJIE WANG (王冰洁),<sup>20,21,22</sup> JOHN R. WEAVER,<sup>11</sup> KATHERINE E. WHITAKER,<sup>11,17</sup> AND ADI ZITRIN<sup>15</sup>

<sup>1</sup>Centre for Astrophysics and Supercomputing, Swinburne University of Technology, Melbourne, VIC 3122, Australia

<sup>2</sup>Department of Astrophysical Sciences, Princeton University, 4 Ivy Lane, Princeton, NJ 08544, USA

<sup>3</sup>Institute of Science and Technology Austria (ISTA), Am Campus 1, Klosterneuburg, Austria

<sup>4</sup>Department of Astronomy, The University of Texas at Austin, Austin, TX 78712, USA

<sup>5</sup>Center for Interdisciplinary Exploration and Research in Astrophysics (CIERA), Northwestern University, IL 60201, USA

<sup>6</sup>Department of Physics and Astronomy and PITT PACC, University of Pittsburgh, Pittsburgh, PA 15260, USA

<sup>7</sup>MIT Kavli Institute for Astrophysics and Space Research, 77 Massachusetts Ave., Cambridge, MA 02139, USA

<sup>8</sup>NSF National Optical-Infrared Astronomy Research Laboratory, 950 North Cherry Avenue, Tucson, AZ 85719, USA

<sup>9</sup>Institut d'Astrophysique de Paris, CNRS, Sorbonne Université, 98bis Boulevard Arago, 75014, Paris, France

<sup>10</sup>Cosmic Dawn Center (DAWN), Niels Bohr Institute, University of Copenhagen, Jagtvej 128, København N, DK-2200, Denmark

<sup>11</sup>Department of Astronomy, University of Massachusetts, Amherst, MA 01003, USA

<sup>12</sup>Kapteyn Astronomical Institute, University of Groningen, P.O. Box 800, 9700 AV Groningen, The Netherlands

<sup>13</sup>Max-Planck-Institut für Astronomie, Königstuhl 17, D-69117, Heidelberg, Germany

<sup>14</sup>Center for Frontier Science, Chiba University, 1-33 Yayoi-cho, Inage-ku, Chiba 263-8522, Japan

<sup>15</sup>Department of Physics, Ben-Gurion University of the Negev, P.O. Box 653, Be'er-Sheva 84105, Israel

<sup>16</sup>Centre for Astrophysics and Supercomputing, Swinburne University of Technology, PO Box 218, Hawthorn, VIC 3122, Australia

<sup>17</sup>Cosmic Dawn Center (DAWN), Denmark

<sup>18</sup>Niels Bohr Institute, University of Copenhagen, Jagtvej 128, 2200 Copenhagen N, Denmark

<sup>19</sup>Department of Astronomy, University of Geneva, Chemin Pegasi 51, 1290 Versoix, Switzerland

<sup>20</sup>Department of Astronomy & Astrophysics, The Pennsylvania State University, University Park, PA 16802, USA

<sup>21</sup>Institute for Computational & Data Sciences, The Pennsylvania State University, University Park, PA 16802, USA

<sup>22</sup>Institute for Gravitation and the Cosmos, The Pennsylvania State University, University Park, PA 16802, USA

<sup>23</sup>Department of Physics & Astronomy, Tufts University, MA 02155, USA

<sup>24</sup>Department for Astrophysical and Planetary Science, University of Colorado, Boulder, CO 80309, USA

<sup>25</sup>Department of Physics and Astronomy, Tufts University, 574 Boston Ave., Medford, MA 02155, USA

<sup>26</sup>Centro de Astrobiología (CAB), CSIC-INTA, Cra. de Ajalvir Km. 4, 28850- Torrejón de Ardoz, Madrid, Spain

<sup>27</sup>Departamento de Física, Faculdade de Ciências, Universidade de Lisboa, Edifício C8, Campo Grande, PT1749-016 Lisbon, Portugal

<sup>28</sup>BNP Paribas Corporate & Institutional Banking, Torre Ocidente Rua Galileu Galilei, 1500-392 Lisbon, Portugal

<sup>29</sup>Kavli Institute for Particle Astrophysics and Cosmology and Department of Physics, Stanford University, Stanford, CA 94305, USA

<sup>30</sup>Astronomy Department, Yale University, 52 Hillhouse Ave, New Haven, CT 06511, USA

(Dated: November 2024)

## ABSTRACT

We present a detailed exploration of the most optically-luminous Little Red Dot ( $L_{\text{H}\alpha} = 10^{44}$  erg/s,  $L_V = 10^{45}$  erg/s,  $F_{444\text{W}} = 22$  AB) discovered by JWST to date. Located in the *UNCOVER* Abell 2744 field, source A2744–45924 was observed by NIRSpec/PRISM with ultradeep spectroscopy reaching  $\langle \text{SNR} \rangle \sim 100 \text{ pix}^{-1}$ , high-resolution  $3 - 4 \mu\text{m}$  NIRCам/Grism spectroscopy from the *All the Little Things* (ALT) program, and multi-band NIRCам Medium Band imaging from *Mega Science*. The NIRCам spectra reveal high rest-frame equivalent width  $W_{\text{H}\alpha,0,\text{broad}} > 800 \text{ \AA}$ , broad  $\text{H}\alpha$  emission (FWHM  $\sim 4500 \text{ km/s}$ ), on top of narrow, complex  $\text{H}\alpha$  absorption. NIRSpec data show exceptionally

strong rest-frame ultraviolet (UV) to near-infrared (NIR) Fe II emission ( $W_{\text{FeII-UV},0} \sim 340 \text{ \AA}$ ), UV N IV]  $\lambda\lambda 1483, 1486$  and N III]  $\lambda 1750$ , and broad NIR O I  $\lambda 8446$  emission. The line spectra unambiguously demonstrate a broad-line region (BLR) associated with a possible  $M_{\text{BH}} \sim 10^9 M_{\odot}$  supermassive black hole embedded in dense gas, which might explain the non-detection in ultradeep Chandra X-ray data ( $\gtrsim 10\times$  underluminous relative to broad  $L_{\text{H}\alpha}$ ). Strong UV Nitrogen lines suggest supersolar N/O ratios due to rapid star formation or intense radiation fields near the AGN. The observed continuum shows a clear Balmer break at rest-frame  $3650 \text{ \AA}$ , which cannot be accounted for by power-law AGN alone. A stellar population model produces an excellent fit with a reddened Balmer break and would imply a massive ( $M_* \approx 8 \times 10^{10} M_{\odot}$ ), old  $\sim 500 \text{ Myr}$ , compact stellar core, among the densest stellar systems known ( $\rho \approx 3 \times 10^6 M_{\odot}/\text{pc}^2$  for  $R_{e,\text{optical}} = 70 \pm 10 \text{ pc}$ ), and AGN emission lines with extreme intrinsic equivalent width  $W_{\text{H}\alpha,0} \gg 1000 \text{ \AA}$ . However, although high  $M_*$  and  $M_{\text{BH}}$  are supported by evidence of a galaxy overdensity containing 40 galaxies at  $z = 4.41 - 4.51$ , deep high-resolution spectroscopy is required to confirm stellar absorption and rule out that the Balmer break is instead caused by dense gas surrounding the AGN.

*Keywords:* Active galactic nuclei (16), High-redshift galaxies (734), Intermediate-mass black holes (816), Early universe (435)

## 1. INTRODUCTION

One of the most exciting findings of *JWST* has been the abundance of high redshift ( $z > 4$ ) active galactic nuclei (AGN; e.g., Harikane et al. 2022; Furtak et al. 2023a; Übler et al. 2023; Larson et al. 2023; Kocevski et al. 2023). Rest-UV selections from the ground have characterized the most massive and rare quasars (e.g., Fan et al. 2023). *JWST* is enabling the discovery of new populations of accreting black holes in up to 10% of the galaxy population at  $4 < z < 7$  (Maiolino et al. 2023; Scholtz et al. 2023) extending to  $z = 10$  (Larson et al. 2023; Kokorev et al. 2023; Goulding et al. 2023). More and more, these high-redshift AGN populations are straining models (Habouzit et al. 2022), both to grow the black holes so early and simultaneously to explain the apparently high ratios of black hole to galaxy mass (e.g., Furtak et al. 2024; Kokorev et al. 2023; Pacucci et al. 2023; Dayal 2024).

We focus here on one particular subset of the new broad-line selected AGN. The combination of red sensitivity and high angular resolution of *JWST* has revealed a population of dust-reddened broad-line AGN (e.g., Kocevski et al. 2023), with high abundances that comprise a few percent of the galaxy population (e.g., Matthee et al. 2024a; Kokorev et al. 2024). In photometry, they are distinguished by a combination of compact morphology and a characteristic “v-shaped” spectral energy distribution (SED), featuring a very red continuum in the

rest-frame optical and faint blue light in the rest UV (Barro et al. 2024; Labbé et al. 2023; Killi et al. 2024; Kocevski et al. 2024). In spectroscopy, they are characterized by prominent broad Balmer lines suggesting dense gas orbiting a supermassive black hole (Matthee et al. 2024a; Greene et al. 2024; Wang et al. 2024a,b). Due to their red color and compact size, they have been dubbed “little red dots” (Matthee et al. 2024a). Photometric selections based on red colors in the rest-frame optical along with compact sizes have been deployed to select large photometric samples of little red dots (e.g., Labbé et al. 2023; Kokorev et al. 2024; Kocevski et al. 2024; Akins et al. 2024). We find a remarkably high incidence of broad Balmer lines in photometrically selected samples (Labbé et al. 2023). Spectroscopic follow-up reveals that  $> 80\%$  of the reddest objects in *JWST* (F277W-F444W  $> 1.7 \text{ AB mag}$ ) also harbor broad lines (Greene et al. 2024; Wang et al. 2024b).

There is not yet a complete picture of the phenomenology of the little red dots. Perhaps we are finding reddened versions of UV-selected quasars (Glikman et al. 2012; Banerji et al. 2015), or very compact dusty starbursts (Pérez-González et al. 2024), or maybe we are probing a new astrophysical phenomenon. An important next step is to characterize the properties of the host galaxies of the little red dots. It is quite challenging to do this robustly, because the sources are so compact and because it is challenging to decompose the spectra into the contributions from galaxy versus AGN light (Wang et al. 2024a; Ma et al. 2024). Fortunately, one of the most luminous and intriguing little red dots, A2744–45924, happens to be behind the A2744 field. Thanks to a range of *JWST* programs, including UNCOVER (Bezanson et al. 2024), Medium Bands, Mega-

\* Brinson Prize Fellow

† NASA Hubble Fellow

‡ Hubble Fellow

§ NHFP Hubble Fellow

Science (Suess et al. 2024), and ALT (Naidu et al. 2024), we have deep NIRCcam imaging for all 20 broad and medium bands, along with F356W grism data at the position of A2744–45924.

In this paper, we highlight one of the brightest (F444W = 22 mag AB) and most H $\alpha$ -luminous little red dots from Labbé et al. (2023) found so far. A2744–45924 is in the Abell 2744 field (R.A.=3.584758, Dec=−30.343630). We will show that this extreme object may have something to teach us about the nature of little red dots more generally. We present the data in §2, the compact galaxy morphology in §3, the fits of the spectral energy distribution in §5, the fits of the emission lines in §4, the quantification of the environment in §7, and the discussion in §8.

Throughout this work, we assume a flat  $\Lambda$ CDM cosmology (e.g. Planck Collaboration et al. 2020) with  $\Omega_{m,0} = 0.3$ ,  $\Omega_{\Lambda,0} = 0.7$  and  $H_0 = 70 \text{ km s}^{-1} \text{ Mpc}^{-1}$ , and a Chabrier (2003) initial mass function (IMF) between  $0.1 - 100 M_{\odot}$ . All magnitudes are expressed in the AB system (Oke & Gunn 1983).

## 2. DATA

### 2.1. UNCOVER Photometry, Spectroscopy, and Lensing Calculations

For spectroscopic targeting, we relied on seven-band NIRCcam photometry and NIRSpec/PRISM spectroscopy taken as part of the Cycle 1 Treasury program Ultradeep NIRSpec and NIRCcam Observations before the Epoch of Reionization (UNCOVER; Bezanson et al. 2024). The UNCOVER data have already yielded exciting new discoveries such as a triply imaged  $z = 7.04$  little red dot (Furtak et al. 2023b, 2024),  $z > 12$  galaxies (Wang et al. 2023), faint galaxies in the epoch of reionization (Atek et al. 2024), and their mass-metallicity relation (Chemerynska et al. 2024), and overdensities at  $z > 7$  (Fujimoto et al. 2023a). We have identified some ALMA bright and *HST*-dark objects (Fujimoto et al. 2023b; Price et al. 2023). Follow-up of objects identified in Labbé et al. (2023) resulted in a dramatic yield of broad lines in little red dots (Greene et al. 2024; Furtak et al. 2024), one at  $z = 8.5$  broad-line AGN (Kokorev et al. 2023), as well as deep spectra of three brown dwarfs (Langeroodi & Hjorth 2023; Burgasser et al. 2024).

UNCOVER imaging was performed over  $45 \text{ arcmin}^2$  in the Hubble Frontier Field (Lotz et al. 2017) cluster Abell 2744, chosen for the large high-magnification area. Original photometry was performed in seven NIRCcam filters (F115W, F150W, F200W, F277W, F356W, F410M, F444W) with 4–6 hour integrations leading to depths of  $\sim 30 \text{ mag}$  (31.5 mag accounting for magnification). Weaver et al. (2024) presents the photometric catalogs,

also including available *HST* data, and the lens model is presented by Furtak et al. (2023c). A2744–45924 was selected from the DR1 images (Labbé et al. 2023). Photometric redshifts are presented by Wang et al. (2024c). The bluest NIRCcam filters (F070W, F090W) were observed by both the Medium Bands, Mega Science (Suess et al. 2024) and ALT (Naidu et al. 2024) surveys, for a total integration time of  $\sim 6\text{--}8 \text{ hr}$  and a depth of  $\sim 30 \text{ mag}$ . Medium Bands, Mega Science also observed all twelve of NIRCcam’s medium-band filters for  $\sim 2.3 \text{ hr}$  each, leading to depths of  $\sim 27.4 - 29 \text{ mag}$  (see Table 1 of Suess et al. 2024). Updated photometric redshift catalogs following the same methods as Weaver et al. (2024) and Wang et al. (2024c) but including new Cycle 2 imaging data are presented in Suess et al. (2024) and publicly available on the UNCOVER website<sup>1</sup>.

A2744–45924 was observed as part of the NIRSpec/PRISM Micro-Shutter Array (MSA) component of UNCOVER (Price et al. 2024). Three of the seven MSA configurations included A2744–45924. The MSA observations employed a 2-POINT-WITH-NIRCcam-SIZE2 dither pattern, and 3 shutter slitlet nod pattern at an aperture angle of  $\sim 44$  degrees. The source was observed in configurations MSA 4, 5, 6, and 7 for a total integration time of 16.3 hours. The PRISM data for each MSA are reduced with *msaexp* (v0.6.10, Brammer 2022). We begin with the level 2 products provided by MAST<sup>2</sup> and then correct for 1/f noise, mask snowballs, and remove the bias on a per-frame basis. WCS, slit-identification and flat-fielding are applied through the *JWST* pipeline, along with photometric correction. Two-dimensional stacked spectra are made by drizzling each MSA observation onto a common grid, aligning, and then stacking them.

The spectra are extracted optimally (e.g., Horne 1986), and flux calibration is performed by convolving the spectrum with the full suite of 20 broad and medium passbands from the combination of UNCOVER (Weaver et al. 2024) and Medium Bands, MegaScience (Suess et al. 2024) and solving for a fifth-order multiplicative polynomial to reproduce the photometry in  $0.''32$  diameter apertures of MegaScience catalog v5.2.0 (Price et al. 2024).

The resulting four spectra are inspected for calibration issues and artifacts. The source was well-centered in MSA 4, but less so in MSA {5, 6, 7}, leading to larger wavelength-dependent photometric corrections. In addition, spectra 5, 6, 7 show spurious discontinuities or un-

<sup>1</sup> <https://jwst-uncover.github.io/>

<sup>2</sup> Available from: <http://dx.doi.org/10.17909/8k5c-xr27>

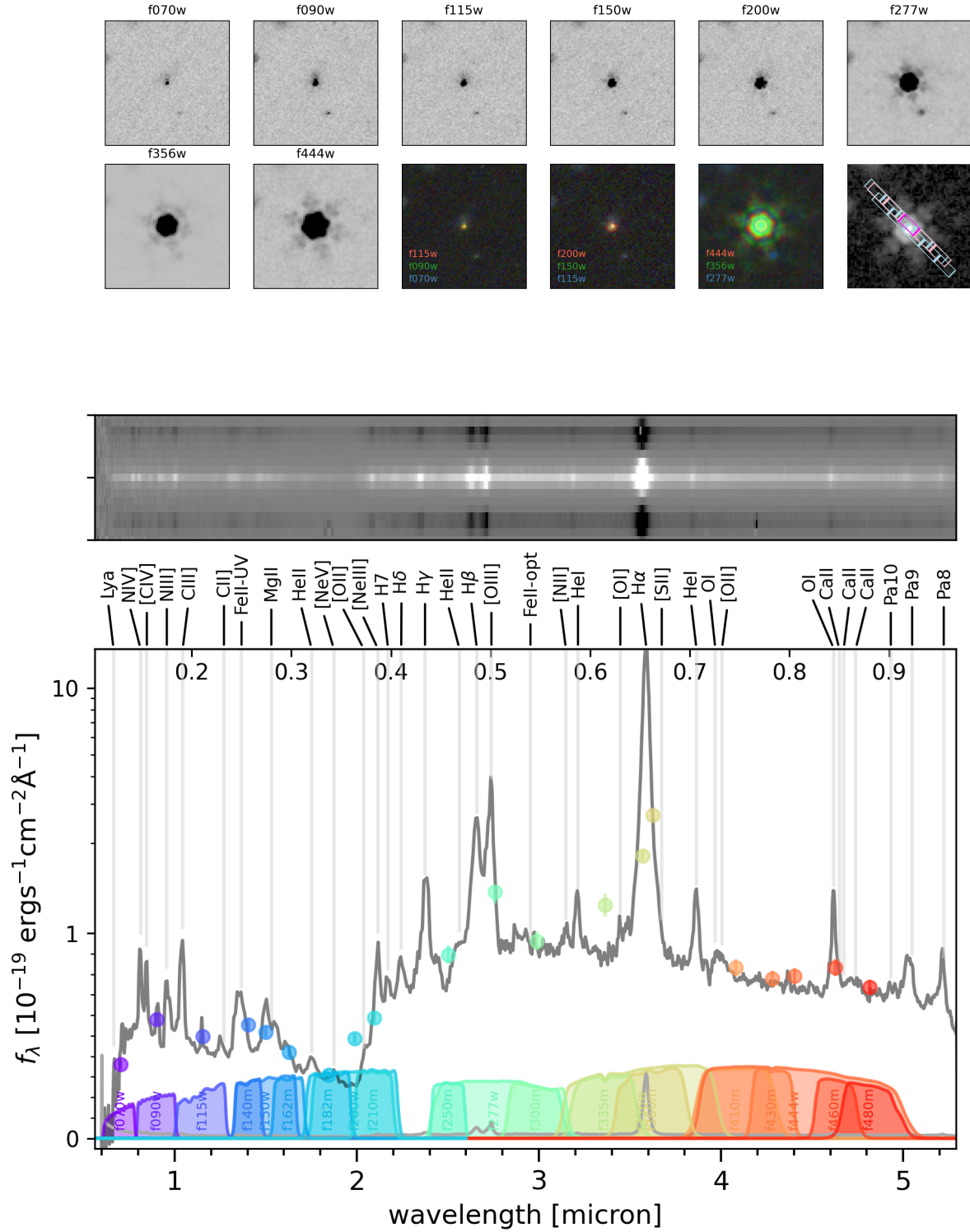


**Figure 1.** Top: broadband NIRCams images of A2744–45924 in the short wavelength channel filters F070W, F090W, F115W, F150W, F200W at 20 mas pixel size and long wavelength channel filters F277W, F356W, F444W at 40 mas pixel size. The images are  $3''$  on a side. North is up, East is left. Also shown are color composite images and an overlay of the micro-shutter array locations of the NIRSpect PRISM observations. Middle: the 2D NIRSpect/PRISM spectrum used for analysis. Bottom: observed NIRSpect/PRISM spectrum (black) and error array (grey). Positions of key spectroscopic features are indicated. Top axis is rest-frame wavelength in micron.

dulations of the continuum at the  $\sim 10\%$  level. These artifacts would not impact the main conclusions of this paper but can affect individual lines and features. Finally, there are small wavelength shifts between the spectra ( $\sim 50\text{\AA}$  at  $3\mu\text{m}$ ;  $0.2\%$ ). These  $\sim 1$  pixel offsets between spectra are similar to those noted in [de Graaff et al. \(2024a\)](#) to arise for compact sources depending on location within the slit (see also [Ferruit et al. 2022](#); [D’Eugenio et al. 2024](#)). To minimize the impact of calibration errors and other systematics on the analysis, we therefore focus on the 4.4 hour spectrum observed on MSA 4 for the remainder of this work. This spectrum has highest S/N of the four,  $S/N = 50 - 200$  per 1D-extracted spectral pixel, sufficient for our purposes, is well-centered in the shutter, well-calibrated, and does not show any obvious artifacts.

Throughout, when we model the NIRSpec/PRISM data, we must forward-model the spectral resolution. In brief, synthetic observations are produced by convolving the model spectra with the NIRSpec/PRISM resolution using published values from JDOX ([Jakobsen et al. 2022](#)) (appropriate for uniformly illuminated slits) increased by a factor 1.3 because our target is a point source. Point sources have considerably better resolution, by up to a factor of  $\approx 2$  ([de Graaff et al. 2024b](#)), but some gains are lost by the large pixel size and processing in the reduction process and coadding of data. The model is then resampled onto the observed wavelength grid with flux conservation.

The magnification of  $\mu = 1.7 \pm 0.2$  for A2744–45924 is calculated based on its position and spectroscopic redshift using the v2.0 UNCOVER strong-lensing model of A2744 from [Furtak et al. \(2023c\)](#), which has been updated with UNCOVER NIRSpec and ALT NIRCам grism spectroscopic redshifts ([Price et al. 2024](#)). This version of the lens model is also publicly available on the UNCOVER website at <https://jwst-uncover.github.io/DR4.html#LensingMaps>.

## 2.2. ALT Survey

The JWST Cycle 2 program All the Little Things (ALT; PID 3516 PIs Matthee & Naidu, [Naidu et al. 2024](#)) observed a mosaic around the Abell 2744 field with NIRCам imaging (F070W, F090W, F356W) and, in particular, grism spectroscopy (GrismR in the F356W filter). The mosaic consists of two sets of four visits, where the two sets are rotated by 5 degrees with respect to each other. These two angles facilitate the removal of contamination and source confusion that is typical for grism spectroscopy. The total on-source integration times range from 6.9–27.2 hours (typically 13.6 hours). The total field of view overlaps with a large

part of the UNCOVER mosaic and yields spectral coverage at  $\lambda = 3.05 - 3.95\mu\text{m}$  with a nominal resolution of  $R \sim 1600$ . Importantly for this paper, this resolution is sufficient to disentangle  $H\alpha$  from  $[\text{N II}]$  emission and measure line width. These data yield spectroscopic redshifts for  $\sim 1600$  galaxies at  $z = 0.3 - 8.5$  (see [Naidu et al. 2024](#) for details on the survey design and analysis).

A2744–45924 is covered by the ALT data with a total on source integration time of 6.9 hours. The grism spectrum in F356W covers rest-frame wavelengths  $0.57\text{--}0.72$  micron at  $z = 4.47$ . The reduction of the grism data and extraction of the two-dimensional spectrum follows the method outlined in [Kashino et al. \(2023\)](#). The continuum level is removed from the spectrum as follows: at a certain wavelength, the continuum level is estimated by calculating the running median over a boxcar filter with a hole around the central wavelength. Similar to [Matthee et al. \(2024a\)](#), we optimize the method to prevent over-subtraction of the broad wings of the lines. We increase the width of the filter and the hole (to 160 and 9 nm, respectively) and explicitly mask  $\pm 5000 \text{ km s}^{-1}$  around the  $H\alpha$  line. The grism spectrum of A2744–45924 is totally uncontaminated in the data from one of the two rotation angles. This allows us to verify the  $H\alpha$  line profile was not modified by the continuum removal procedure. The one-dimensional spectrum is optimally extracted (e.g., [Horne 1986](#)) using a Gaussian fit to the spatial extent of the spectrum collapsed over the  $H\alpha$  wavelength. The typical rms noise level of the spectrum is  $6 \times 10^{-20} \text{ erg s}^{-1} \text{ cm}^{-2} \text{ \AA}^{-1}$ .

## 3. MORPHOLOGY

Initial visual inspection of the images in Figure 1 shows two distinct components: a main compact source and blue diffuse emission extending to the North. To quantify the morphology of the source we perform Sérsic profile fitting to the images using the package *pysersic* ([Pasha & Miller 2023](#)). We focus on three bands: F070W representing the rest-far-UV continuum (although note that the full band extends blueward of  $\text{Ly}\alpha$ ), F200W near the  $4000\text{\AA}$  break, and F300M for the line-free optical continuum. We use cutouts from the mosaics, weight maps and Point Spread Functions presented in [Suess et al. \(2024\)](#) using methods presented in [Weaver et al. \(2024\)](#). We use the native pixel scale of  $0.02 \text{ arcsec/pixel}$  for the F070W and F200W images, and the  $0.04 \text{ arcsec/pixel}$  scale for F300M. In order to not bias the measurements of the main bright compact source we perform a two component fit, where both are Sérsic profiles, with the second component representing the nearby low-surface brightness emission seen in the SW filters. We employ a double Sérsic model in order

to determine whether the core is resolved or unresolved. For each band we sample the posterior distributions for the parameters using a No U-Turn sampler (Hoffman et al. 2014; Phan et al. 2019), with 2 chains for 1000 warm-up steps and 2000 sampling steps each. To ensure robust sampling we re-parameterize variables using a multivariate normal distribution fit to the posterior, following Hoffman et al. (2019). We test to make sure the results converge by ensuring the  $\hat{r}$  metric and effective sample size are  $< 1.02$  and  $> 400$  respectively for the parameters of interest (Vehtari et al. 2021).

From these two component fits, the light is dominated at all wavelengths by the central compact component (Figure 2), which is centered in the MSA slit (Figure 1). This compact component appears to be marginally resolved in the F070W and F200W filters, but is completely point-like in F444W. We did attempt a two-component fit to the F444W image, but the second component was completely unconstrained (see also Chen et al. 2024). As we will argue in §5.2, the spectrum is dominated by Balmer break feature in the F200W band, and therefore we derive the structural measurements from this band. We measure a size at F200W of  $r_e = 0.010 \pm 0.001''$  and a similar size for F300M. F300M is useful as it avoids strong emission lines and provides a clean measurement of the rest-frame optical continuum  $0.55\mu\text{m}$ . However, from extensive testing of size limits with stars in Labbé et al. (2023), we find that we cannot reliably measure sizes below a third of a pixel. Given  $0.04''$  pixels, we find a magnification-corrected size of  $r_e \lesssim 70 \pm 10$  pc for the primary compact component to the South.

The second extended component towards the North is both fainter and bluer than the primary component. At F070W, the component is quite diffuse, but in the F090W and F115W images the second component is clearly visible (Figure 1). Fitting this component at F070W, we find an extended blue component with  $n \approx 1$  and  $r_e \approx 0.16''$ ; the Northern component is asymmetric and only falls partially within the MSA. The angular size corresponds to  $r_e \approx 700$  pc (accounting for lensing), if it is present at the same redshift as the main source. The Northern source is barely detected in F200W, and becomes undetectable redward. Unfortunately, the grism data are not sensitive enough in the blue to detect the extended component. The resolution is also growing worse redward of F200W and the very prominent point-source dominates the total light.

The presence of extended blue emission on hundreds of parsec scales seems to argue for star-light dominating the UV continuum. With a surface brightness of  $23.5$  mag arcsec $^{-2}$ , the level is much brighter than would

be expected from scattered light, if scaling from lower-redshift analogs at similar intrinsic luminosity (Zakamska et al. 2006). On the other hand, it is possible that the extended emission comes from lines like Ly $\alpha$ , photoionized by the same source that ionizes the H $\alpha$ . Taking the integrated flux from the extended component, we find a luminosity of  $L \approx 6 \times 10^{43}$  erg/s, which is very similar to the H $\alpha$  luminosity (see §4.3). Thus, assuming Case B recombination, perhaps  $\sim 10\%$  of the Ly $\alpha$  has scattered into this extended component. Future integral-field data could determine the nature of the Northern component, and particularly whether Mg II and other resonant lines also contribute.

## 4. EMISSION LINES

### 4.1. Far-UV Emission Line Fits

The NIRSpec/PRISM spectra cover from  $0.7 - 5\mu\text{m}$  observed, which probes from Ly $\alpha$  to beyond H $\alpha$  at  $z = 4.47$ . Note that the PRISM has high sensitivity but low dispersion, with  $R = 50 - 400$  across the wavelength coverage for a point source (de Graaff et al. 2024b). In this section we present new fits to the rest-UV lines (Treiber et al. 2024).

We fit the region from 1280-2110Å rest-frame with the combination of a power-law ( $f_\lambda \propto \lambda^\beta$ ) and emission lines: N IV]  $\lambda 1488$ , C IV  $\lambda 1549$ , He II  $\lambda 1640$ , O III]  $\lambda 1666$ , N III]  $\lambda 1750$ , Si III]  $\lambda 1888$ , and C III]  $\lambda 1909$  (Figure 3). We also include the blend of AlIII  $\lambda 1860$ , [Ne III]+Si II  $\lambda 1815$  and Fe II  $\lambda 1786$  next to N III]. See Table 5 for rest wavelengths and fluxes. In the UV, where  $R \sim 50 - 100$ , we have weak constraints on the line widths. Nominally the fits prefer line-widths greater than 2000 km/s.

With the instrument-model thus constructed, we then create an oversampled but variable wavelength grid in order to handle the variable resolution. We convolve the model Gaussians with the instrument model as described in §2.1. Our fit is presented in Figure 3. All strong UV lines are well-detected, including the blend of AlIII, [Ne III]+Si II and Fe II next to N III] (Shen et al. 2019). Without these lines, there was a clear excess in the fit. The line equivalent widths are among the highest observed in UV emission lines in the UNCOVER/PRISM UV-line emitter sample at  $z > 3$  (Treiber et al. 2024). The fluxes are reported in Table 2.

Treiber et al. (2024) also investigate the location of A2744–45924 in UV diagnostic diagrams, finding that the line ratios are in the region of these diagrams occupied both by broad UV emission lines in quasars and by star-forming galaxies. Based on the detection of broad Fe II presented in §4.2, we favor the hypothesis that the

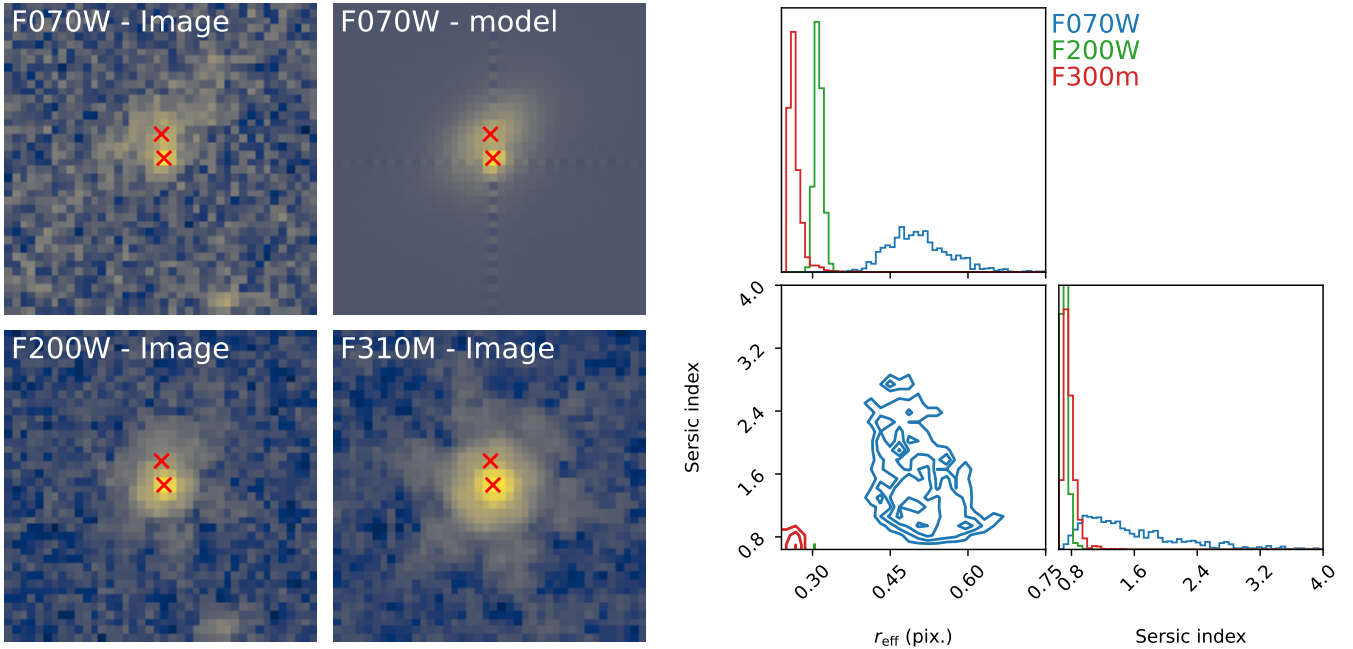


**Figure 2.** Results of fitting two-component models to the F070W, F200W, and F300M images of A2744–45924 using `pysersic`, orientation has North up as above in Figure 1. We show zoomed in cutouts of the three bands modeling alongside the joint posterior distribution of the Sersic index and effective radius for the bright compact component. We find that A2744–45924 is marginally resolved in F070W and F200W, but point-like at longer wavelengths. We adopt the F200W size, as it is most likely to be dominated by evolved stars §5.2.

UV emission lines also emerge from the broad-line region. First, we discuss the strong Nitrogen lines also detected in the rest-frame UV.

#### 4.1.1. Strong Nitrogen emitter

We detect N IV] $\lambda\lambda$ 1483, 1486 with an equivalent width of 25 Å and N III] $\lambda$ 1750 with an equivalent width of 30 Å in the A2744–45924 spectrum. N IV] is seen in narrow-line AGN selected in the UV and optical (see the stacks in Hainline et al. 2011; Alexandroff et al. 2018), while Le Fèvre et al. (2019) and Sobral et al. (2018) present AGN stacks with Ly $\alpha$  and CIII] emission that show N III]. In contrast, these two lines are rarely seen in broad-line AGN ( $< 1\%$  in SDSS Bentz et al. 2004; Glikman et al. 2007). In the rare SDSS quasars with strong N IV] and N III], the elevated equivalent widths seem to suggest super-solar abundance ratios of N/O (e.g., Jiang et al. 2008), although Batra & Baldwin (2014) present an alternate interpretation of high overall metallicity. Interestingly, the incidence of luminous radio activity is much higher among the N-emitting quasars (e.g., Humphrey et al. 2008; Jiang et al. 2008), perhaps suggesting either that shock excitation is part of the strong Nitrogen emission, or that there is an evolutionary link between radio activity and Nitrogen emission; a search for radio emission from A2744–45924 could be quite interesting, although in a stack of hundreds of photometrically se-

lected little red dots, no radio continuum is detected (Akens et al. 2024). Finally, we note that N IV] is also detected in the prototypical narrow-line AGN NGC 1068 (Kraemer & Crenshaw 2000). In that case, photoionization modeling does a very good job reproducing nearly all the UV/optical emission lines, but models with supersolar N/O tuned to reproduce N V tend to overproduce N IV]. In other words, it can be challenging to model the Nitrogen lines in even nearby AGN.

Before *JWST*, very few star-forming galaxies had been seen to have the N IV] line, either local dwarf starbursts (Berg et al. 2022) or high-redshift lensed systems (Fosbury et al. 2003; Raiter et al. 2010). Now, more such galaxies are emerging at high redshift (e.g., Bunker et al. 2023; Topping et al. 2024; Isobe et al. 2023; Barchiesi et al. 2023; Marques-Chaves et al. 2024). It is not yet clear in individual cases whether an AGN is needed to supply the hard ionizing radiation needed to excite the N IV]. Other explanations relate more directly to the massive stars associated with the observed starbursts. For instance, Cameron et al. (2023) explore scenarios in which stellar collisions or tidal disruption events might pollute the ISM with extra Nitrogen produced in the CNO cycle (see also Senchyna et al. 2024). Higher spectral resolution data are needed to decouple broad and narrow lines, as well as to measure line ratios of the N

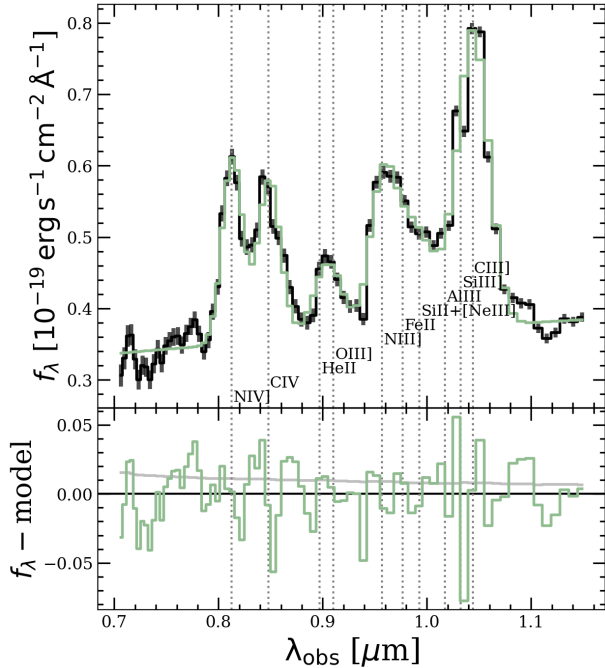


**Figure 3.** Rest-frame far-UV fit to A2744–45924. We see prominent N IV]  $\lambda 1483$  + N IV]  $\lambda 1487$  Å, CIV  $\lambda \lambda 1548, 1551$ , He II  $\lambda 1640$ , O III]  $\lambda \lambda 1661, 1666$ , N III]  $\lambda 1750$ , and [C III]  $\lambda 1907$  + [C III]  $\lambda 1909$ . Note that Si III] and C III] are blended, as are He II and O III]. Also needed to explain the spectrum is the blend of Al III  $\lambda 1860$ , [Ne III] + Si II  $\lambda 1815$  and Fe II  $\lambda 1786$ , which are lines also found in the Shen et al. (2019)  $z \gtrsim 5.7$  quasar composite. This broad-line fit is marginally preferred over fits constrained to narrower FWHM. The CIV profile drives this preference, which may be because of the blending in most other lines or because CIV alone is broad. We show the broad fit because of this fit preference and the evidence from Fe II of broad-line emission in the rest-frame UV.

lines themselves. These data will allow for detailed photoionization modeling and shed new light on the origin of the Nitrogen lines in A2744–45924.

#### 4.2. Near-UV Emission line fits

The rest-frame near UV 2000 – 3200 Å shows a complex aggregate of emission lines around Mg II  $\lambda 2798$  which we identify as broad Fe II line emission. Fe II emission is common in broad-line AGN (Osterbrock 1977) and can be a prominent contributor to the UV, optical, and NIR emission line spectrum in AGN (Wills et al. 1985; Boroson & Green 1992; Rodriguez et al. 2002). Iron emission is thought to originate in the outer parts of the broad line region (BLR) (Kovačević et al. 2010), with a shape and equivalent width reflecting the physical conditions of BLR clouds (Baldwin et al. 2004), and the equivalent width is suggested to correlate with

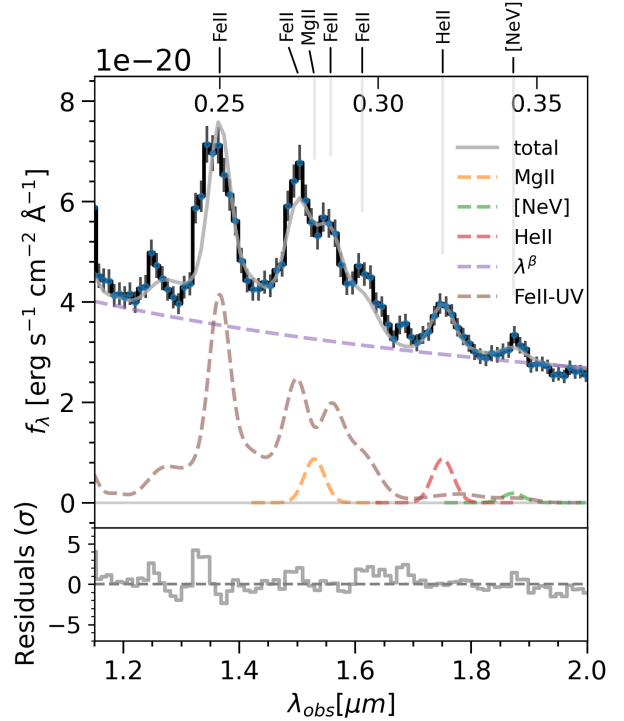


**Figure 4.** Model fits to the rest-frame near-UV. Shown are the observations (black solid line), the local AGN powerlaw continuum (purple dashed), strong broad-line Fe II pseudo-continuum emission (brown dashed) and the broad Mg II  $\lambda 2798$  (yellow), broad He II  $\lambda 3203$  (red), and narrow [Ne V]  $\lambda 3426$  (green) emission lines.

the relative black hole accretion rate (Boroson & Green 1992).

The challenge in modeling the Fe II emission complex is that the Fe<sup>+</sup> ion emits through thousands of emission line multiplets that blend together to form a pseudo continuum. Typically, the Fe II is modeled using empirical templates from low-redshift, well-studied sources (e.g., Vestergaard & Wilkes 2001). Here we use empirical templates based on the Seyfert 1 galaxy I Zwicky 1, divided into sections to allow more flexibility in reproducing the shape of the observed emission: below 2000 Å the template of Vestergaard & Wilkes (2001) is used, at 2200 – 2400 Å, 2400 – 2600 Å, and 2650 – 3090 Å the template of Salvander et al. (2006), which models the flux underneath Mg II, and from 3090 – 3600 Å the template of Tsuzuki et al. (2006). The Fe II line templates are convolved with a Gaussian to match the width of the broad line H $\alpha$  (see §4.3).

To model the near-UV from 2000 – 3600 Å, we fit a combination of a power law, the Fe II templates, and the Mg II  $\lambda 2798$ , He II  $\lambda 3203$ , and [Ne V]  $\lambda 3426$  emission lines, assuming Gaussian profiles, with NIRSspec PRISM observations modeled as above. At 1.5  $\mu$ m the effective resolution of NIRSspec is only  $R \sim 40$ , so individual lines

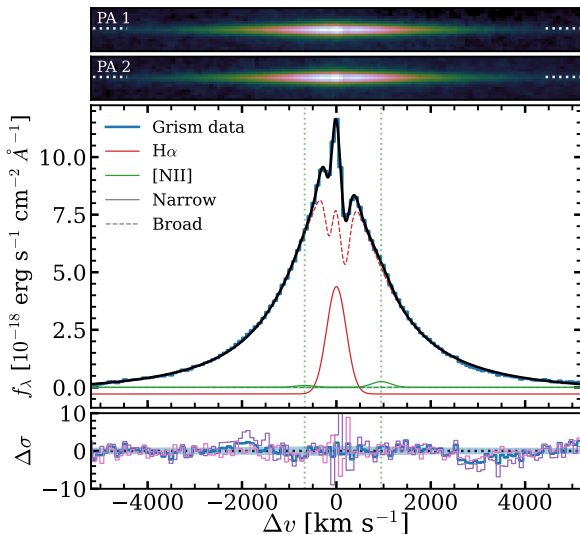


**Figure 5.** The total  $\text{H}\alpha + [\text{N II}]$  emission line profile as seen by the JWST/F356W GrismR with best-fit line emission and absorption complex. The profile is centered on the central velocity of the broad  $\text{H}\alpha$  component. Green dashed lines mark the location of the  $[\text{N II}]$  doublet. The top panels show the two-dimensional grism spectrum from each roll angle with a  $\gamma = 0.5$  power-law normalisation to highlight the dynamic range in the data. The bottom panel shows the residuals of the best fit, normalised by the noise level. In pink and purple we show the residuals from individual roll angles, while in blue we show the residuals from the average of both roll angles.

are unresolved. As shown in Figure 4 all lines are clearly detected. The permitted Fe II, Mg II, and He II are common BLR lines, and the narrow line  $[\text{Ne V}] \lambda 3426$  is a strong indicator of AGN accretion due to its high ionization potential (e.g., Abel & Satyapal 2008; Chisholm et al. 2024). We estimate the equivalent width of Fe II, by integrating the flux between 2200 – 3050 Å, relative to the powerlaw continuum. The measurements are presented in Table 3. The Fe II-UV emission is exceptionally strong, with rest-frame equivalent width  $W_{\text{FeII-UV}} \sim 340$  Å. For comparison, the largest EW measured in a sample of 4178 Seyfert 1 galaxies and QSOs in SDSS at  $z < 0.8$  is  $W_{\text{FeII-UV}} \sim 400$  Å (Dong et al. 2011), with only 0.07% of AGN exceeding 300 Å.

We also present fits to the rest-frame optical and NIR lines from the PRISM data in Appendix A. Some noteworthy findings include broad He II  $\lambda 4686$ , broad Balmer, broad O I  $\lambda 8446$ , tentative broad Ca II triplet lines, and the broad Fe II  $\lambda 9200$  bump in emission, indicating widespread high equivalent width BLR line emission throughout the UV-optical-NIR spectrum.

#### 4.3. ALT Optical Emission Line Fits

We fit the one-dimensional  $\text{H}\alpha$  profile measured in the NIRC2 grism data with the same methodology as used in Matthee et al. (2024a), which means that we simultaneously fit for a narrow component for  $\text{H}\alpha$  and  $[\text{N II}]$  (fixing the  $[\text{N II}] \lambda 6549, 6585$  doublet ratio to 1:2.94 as set by quantum mechanics), a broad  $\text{H}\alpha$  wing, and  $\text{H}\alpha$  absorption components. We include the data from  $\lambda_0 = 6420 - 6680$  Å in the fit and use a least squares minimizer implemented in the `lmfit` package.

The  $\text{H}\alpha + [\text{N II}]$  line profile is quite complex (Figure 5). To describe the wings of the  $\text{H}\alpha$  line, we use a Lorentzian function with a  $\text{FWHM} = 4540 \pm 50$  km/s which is strongly preferred over a Gaussian profile. Then, in order to model the narrow  $\text{H}\alpha$  and  $[\text{N II}]$  components, we include a Gaussian component at the position of  $\text{H}\alpha$  and the  $[\text{N II}]$  doublet with best-fit  $\text{FWHM} = 460 \pm 30$  km/s. The widths of the narrow components are fixed to each other. There is no significant velocity offset between the narrow and broad component. The best-fit  $[\text{N II}]/\text{H}\alpha$  ratio of the narrow component is  $0.02 \pm 0.02$ , i.e. no significant  $[\text{N II}]$  emission is detected. The very low ratio of  $[\text{N II}]/\text{H}\alpha$  is not dependent on the absorber velocities or strengths (see below), as they are far from the  $[\text{N II}]$  in velocity. Thus, we find a genuine low ratio of  $[\text{N II}]/\text{H}\alpha$ , which typically implies low gas-phase metallicities (e.g., Groves et al. 2006).

After trying a number of configurations, we find that the best overall fit is achieved with two additional absorption components at  $-143$  and  $+172$  km/s from the systemic velocity set by the broad  $\text{H}\alpha$  component. The absorption lines are barely spectroscopically resolved ( $\text{FWHMs}$  of 240-330 km s $^{-1}$ ) and their rest-frame equivalent widths are 1.2-2.0 and 2.3-4.4 Å. The fit is significantly preferred compared to a fit with no absorbers ( $\Delta\chi^2 = 11$ ) and with a single absorber ( $\Delta\chi^2 = 4.4$ ). However, there is significant degeneracy between the width and strength of the narrow  $\text{H}\alpha$  and the width and equivalent width of the absorbers. If we had high-resolution coverage of  $[\text{O III}]$  we would be able to break this degeneracy. For now, we simply argue that absorption features are needed, and defer quantitative analysis of these lines until multiple transitions can be observed at high resolution.

The best-fit profile has a reduced  $\chi^2 = 2.4$ . The residuals, shown in the bottom panel of Fig. 5, are relatively free of correlated structure, in particular after the addition of the absorbing components and using a Lorentzian broad component. Some large-scale skewness can be identified over the  $-2000$  to  $2000$  km s $^{-1}$  range, which could either be indicative of a third line-profile component (such as an outflow), or could be a result of a degeneracy with the centroiding of the broad component

with the complex absorption near line-center. A higher resolution spectrum is required for even more complex modeling. We will revisit the implications of the Balmer absorption lines in §8.

Finally, we note that data in separate roll angles yield fully consistent profiles. The complexity therefore is truly from the line-profile and not due to the spatial-spectral degeneracy of grism data. Multiple narrow or broad components without absorption are far less successful at yielding a good fit to the data, in particular due the strong symmetry of the broad wings of the line. Thus, despite significant degeneracy in fitting the narrow components on top of the absorption, the broad line width and flux are quite robust, as well as reassuringly consistent with the original PRISM fit (Greene et al. 2024).

## 5. SPECTRAL ENERGY DISTRIBUTION FITS

A defining property of the little red dots is the “v-shaped” spectrum, consisting of a red rest-frame optical continuum and a blue rest-frame UV continuum (e.g., Labbé et al. 2023; Kocevski et al. 2024). However, as more and more LRD spectra become available, it has become increasingly clear that the transition from red to blue continuum often occurs at  $\lambda_{\text{break}} \approx 3600 \text{ \AA}$ , and in some cases there is a defined break in the continuum shape that resembles a Balmer break (Wang et al. 2024a,b; Setton et al. 2024).

In the case of A2744–45924, there is clear evidence of a sharp and large Balmer Break at  $3650 \text{ \AA}$ , suggesting the presence of an evolved stellar population. At the same time, the broad and high EW Fe II in the UV and NIR, and broad H $\alpha$  in the optical suggest that AGN continuum might contribute significantly at wavelengths blueward and redward of the break. If the Balmer Break is stellar in origin (but see Inayoshi & Maiolino (2024) for an alternate explanation), any fit to the full spectrum using current models thus requires similar contributions from an AGN continuum with strong emission lines and an evolved stellar population. Joint modeling of a composite AGN, along with a stellar component is a delicate procedure (Akins et al. 2023; Wang et al. 2024a). Because of the many independent components, it is hard to be sure that the solutions are unique. The SNR of A2744–45924 is by far the highest amongst the population of little red dots with spectroscopic follow-up, offering the opportunity to disentangle the AGN and stellar components.

### 5.1. AGN and Stellar SED models

We first describe a flexible AGN model with ingredients based on known UV-selected AGN, and including

a range of BLR emission line components seen in the spectrum of A2744–45924. The model has the following components:

- A power-law continuum,  $\lambda^\beta$ , parameterized by slope  $\beta$  and luminosity.
- Balmer series emission lines, with relative emission line strengths fixed to Case B line ratios<sup>3</sup>:
  - a broad Balmer series, set to the FWHM of the broad H $\alpha$  line. The strengths of the broad Balmer lines are tied to the AGN power-law continuum via the equivalent width of H $\alpha$ .
  - a secondary narrow Balmer series component, set to the FWHM of [O III], with free normalization.
- [O II], [Ne III] $\lambda 3867$ , and [O III]  $\lambda\lambda 4960, 5008$  doublet emission lines, each set to the FWHM of [O III] and modeled as free parameters. The [O III] doublet line ratio is set to 1:3.
- Fe II lines using a combination of templates. Originating in the broad-line region, these lines are numerous enough to form a “pseudo-continuum” after convolution to the FWHM of H $\alpha$ :
  - empirical templates, based on the Seyfert 1 galaxy I Zwicky 1 (e.g., Vestergaard & Wilkes 2001; Tsuzuki et al. 2006; Boroson & Green 1992; Véron-Cetty et al. 2004). The relatively narrow broad lines of I Zwicky 1 facilitate matching to the observed FWHM after convolution.
  - flexible theoretical templates from Kovačević et al. (2010), which combines the strongest Fe II multiplets in three groups.
- Additional far-UV, optical, and near-IR broad and narrow lines specific to AGN, modeled as Gaussians (full list provided in Table 5).
- AGN dust attenuation, modeled as a power law, with the index shared with the stellar population component.

The AGN model has the following free parameters: continuum slope  $\beta$ , continuum luminosity, EW H $\alpha_{\text{broad}}$ ,

<sup>3</sup> Fixing the Balmer line ratios helps mitigate degeneracies at  $< 4100 \text{ \AA}$ , where the low resolution of NIRSpec/PRISM blends lines into a pseudo-continuum ending at  $3650 \text{ \AA}$ , resembling a Balmer Break.

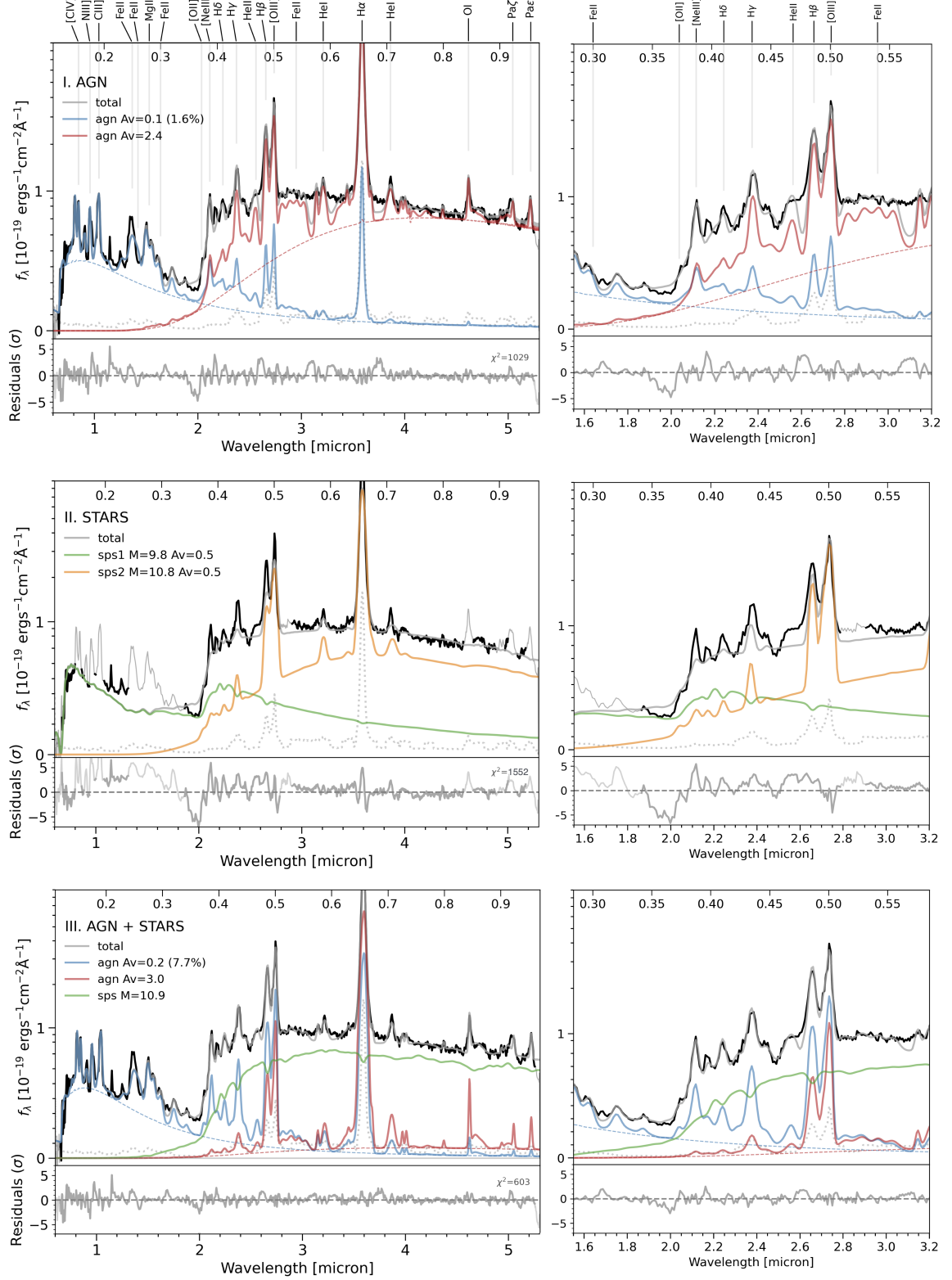


**Figure 6.** Model fitting results using only AGN components (model I, top panels), only stellar components (model II, middle), and a mix of AGN and stars (model III, bottom). NIRSspec/PRISM observations (black), uncertainties (dotted), model fits (gray), and normalized residuals are shown. Model I consists of a dust-reddened AGN component (red) and a blue component (here parameterized as a fraction of dust-free scattered light; blue), which dominates at  $< 2\mu\text{m}$  despite being only a small percentage of the red luminosity. The model can produce an apparent sharp break at  $\sim 3500\text{\AA}$  due to a blend of strong broad emission lines and broad Fe II pseudo-continuum at  $4000 - 5500\text{\AA}$ , but leaves significant residuals throughout the rest-frame optical. Model II consists of two FSPS population components, each velocity-broadened according to the stellar mass and effective radius at F300W and where the broad lines are stellar in origin. AGN specific lines are masked. Model III is a mix of AGN and a stellar component. This fit prefers an evolved stellar population to dominating the rest-frame optical to match the observed Balmer break, with significant contribution from AGN emission lines and Fe II. Between these models, model III is favored by the data.

$L_{\text{H}\alpha_{\text{narrow}}}$ ,  $A_{\text{V,AGN}}$  and dust index, UV-optical-NIR broad and narrow lines, and Fe II width and amplitude.

To model the stellar continuum, we use FSPS stellar population models (Conroy & Gunn 2010) based on a Chabrier (2003) IMF,  $0.1 - 2.0Z_{\odot}$  metallicity, and delayed- $\tau$  star formation histories (SFH). Note that strong constraints on metallicity and SFH are difficult to achieve in the presence of significant AGN contributions at all wavelengths. Some additional flexibility in SFH can be achieved by allowing a two component stellar population model (e.g., young burst and older population), but we do not explore more freedom in these parameters, e.g., “non-parametric” star formation histories (Leja et al. 2019) or attempt to interpret the best-fit ages. Dust attenuation is modeled as a power law with a variable slope with the same index as the AGN dust. Each stellar population component has six free parameters: stellar mass, metallicity,  $\tau$ , age,  $A_{\text{V,sps}}$ , and ionization parameter  $U$ .

We note that our approach shares many similarities with other works attempting to model the rest-frame UV/optical spectra of little red dots with prominent apparent breaks, in particular Wang et al. (2024a,b) and Ma et al. (2024). The AGN models, and the treatment of dust attenuation, are quite similar across these works. As in Ma et al. (2024), when tying the dust slopes for the AGN and the galaxy together, we find quite steep slopes ( $\delta = -1.8$ ), and as in both Ma et al. and Wang et al. we find it difficult to reproduce the break with smooth power-law AGN components alone.

The observed spectrum has a very high SNR, but the effective SNR is limited by calibration and other systematic uncertainties. We therefore set a systematic uncertainty floor of 5% of the flux, added in quadrature to the Poisson noise, comparable to systematic uncertainties in the photometry. At the location of strong lines we increase the value to 10% to account for additional systematics in the line modeling (e.g., line spread function, wavelength calibration, line center and shape etc, as these details are not explicitly modeled). In cases that emission lines are not modeled, we mask them. Posterior distributions are sampled with `pymultinest` (Buchner et al. 2019; Feroz et al. 2010). Model parameters, priors, and posteriors are in Table 1.

## 5.2. Stellar and AGN Continuum fits

We proceed with fitting three models, one with only AGN components (I), one with only stellar components (II), and one with a mix of stars and AGN (III).

### 5.2.1. I. AGN only

From the spectrum of A2744–45924 it is apparent two AGN components are needed: a blue AGN continuum

**Table 1.** Continuum Fits

Var.	Model I	Model II	Model III
$\chi^2$	1029	1552	603
$n_{\text{DOF}}$	649	520	644
$\ln Z$	$-588 \pm 0.5$	$-931 \pm 0.5$	$-400 \pm 0.8$
dust			
dust index	$-1.79 \pm 0.01$	$-1.79 \pm 0.01$	$-1.79 \pm 0.01$
AGN			
$\log L_0$	$12.56 \pm 0.01$	...	$12.23 \pm 0.06$
$\log L_s$	$10.82 \pm 0.01$	...	$11.02 \pm 0.02$
$\beta$	$-2.2 \pm 0.01$	...	$-2.90 \pm 0.05$
$\log \text{EW}_b$	$2.99 \pm 0.02$	...	$3.75 \pm 0.04$
$\log \text{EW}_n$	$2.82 \pm 0.03$	...	$3.48 \pm 0.04$
$A_V$	$2.40 \pm 0.02$	...	$3.0 \pm 0.2$
$A_{V,s}$	$0.1 \pm 0.01$	...	$0.2 \pm 0.01$
Gal (primary)			
$\log M_*$	...	$10.8 \pm 0.1$	$10.9 \pm 0.02$
$\log \tau$	...	$7.3 \pm 0.3$	$6.9 \pm 0.3$
$\log t$	...	$7.4 \pm 0.5$	$8.7 \pm 0.01$
$[Z/H]$	...	$-1 \pm 0.01$	$0.28 \pm 0.02$
$A_V$	...	$2.5 \pm 0.02$	$1.17 \pm 0.04$
Gal (blue)			
$\log M_*$	...	$9.83 \pm 0.03$	...
$\log t$	...	$8.74 \pm 0.04$	...
$A_V$	...	$0.005 \pm 0.007$	...

NOTE—Luminosities and stellar masses are corrected for the lensing magnification  $\mu = 1.7 \pm 0.2$ . The AGN  $\text{H}\alpha$  rest-frame equivalent widths are computed relative to the AGN powerlaw continuum. Note: the uncertainties on dust index and age are artificially small because they run into the limits of the prior. In general, all quoted uncertainties should be considered underestimates and much smaller than the expected systematics.

to explain the blue UV spectrum, and a reddened AGN to represent the red part of the spectrum (with a cross-over point near the Balmer break region). To keep the number of free parameters small, we couple the AGN models so that the blue AGN is simply some dust-free fraction of the reddened AGN model, effectively introducing one extra free parameter  $f_{\text{blue}}$ . In this model the blue AGN can be thought of as a fraction of dust-scattered light escaping without reddening. The fit is presented in the top row of Figure 6. While the model is able to reproduce certain features well, including the complex emission complex in the UV and the overall shape of the SED, two clear discrepancies are visible: 1) a large mismatch around the Balmer break, indicating that the underlying power-law AGN continuum model is too smooth, and related 2) large oscillating residuals at  $0.36 - 0.7\mu\text{m}$ , due to strong emission lines and Fe II pseudo-continuum attempting to make up for the con-

tinuum model mismatch. The mismatch is especially apparent in regions where Fe II is known to be weak or absent; here the residuals are largest. Another notable aspect of the model is the need for a large negative dust law index  $\alpha = -1.8$  reflecting large reddening around the break, but low reddening at longer wavelengths. This is likely another expression of the fundamental mismatch between a powerlaw continuum of the model and the large observed break in the observed spectrum. Despite the reasonably conservative errors of 5–10% per pixel, the formal fit is rather poor  $\chi^2_{red} = 1.6$ .

### 5.2.2. II. Stars only

Next we model the spectrum with only stellar population models. Like above, we include two stellar models, a low-dust model  $A_V < 1$  to reflect the UV light, and  $A_V > 1$  model for the red. The star formation histories are independent, allowing significantly more freedom in the combined SFH (e.g., a young burst on top of an older stellar population). Strong Fe II features are masked, as these are not produced in the FSPS models. Line widths are assumed to be due to virial motion of the stars. The stellar model is convolved with a velocity dispersion parameterized by the stellar mass and a size  $r_e = 70\text{pc}$  (see §3) following the relation by (van Dokkum et al. 2015). As shown by Baggen et al. (2024), extremely compact sizes and large stellar masses  $\log(M/M_\odot) > 10$  can produce line widths of 1000s km/s, similar to observed. The results are shown in the middle row of Figure 6. As with the AGN only model, some aspects of the observations can be reproduced, including the overall shape and broad lines, but the fit is poor  $\chi^2_{red} = 3.0$ . The model does a better job at matching the continuum at  $0.5 - 0.7\mu\text{m}$ , but shows large residuals around the Balmer break and at  $0.4 - 0.5\mu\text{m}$ , where Fe II lines contribute. Some of the mismatch could be due to restrictions in the combination of SFH and dust (e.g., a dust-reddened post-starburst population without emission lines could be added). But this exercise is meant to show that the most straightforward and reasonably simple models do not reproduce the full spectrum of A2744–45924. Obviously, the stellar-only model is incapable of producing AGN-specific BLR lines.

### 5.2.3. III. Stars + AGN

Finally, we attempt a model containing both AGN continuum (two components as in model I) and a stellar population. The motivation is that the high EW of the Fe II $\lambda$ 2500, Fe II $\lambda$ 9200, and H $\alpha$  suggest that the rest-frame  $0.1 - 0.3\mu\text{m}$  and  $0.6 - 1.0\mu\text{m}$  are AGN dominated, while the rest-frame optical  $0.3 - 0.6\mu\text{m}$  could be dominated by a stellar population producing the Balmer break (e.g., Wang et al. 2024b; Baggen et al. 2024). As

shown in Figure 6 (*bottom panels*) this model indeed is a much better fit  $\chi^2_{red} = 0.9$ . To see which of the three models is favored by the data we can use the evidence produced by the multineest fitting procedure. Comparing with the simpler AGN-only model I, we compute the Bayes Factor (the ratio of the logarithm of the evidence  $Z$ ) to see if the added complexity of model III is justified by the data.  $Z$  is the probability of the data given the model, marginalized over the model parameter space. It accounts for model complexity, favoring simpler models unless the data strongly supports the added complexity. We find  $\ln(B_{I,III}) = \ln(Z_I/Z_{III}) = -81$ , indicating strong evidence for model III. The conclusion from the SED fitting is that AGN power-law continua do not provide a good description of the data, and that a model component is required that produces a strong optical continuum break. In the context of the models considered here, this suggests a stellar-dominated optical continuum, with inferred  $M_* \sim 8 \times 10^{10} M_\odot$  in stars, an age of  $\sim 500$  Myr and significant attenuation  $A_V \sim 1$ . In Appendix B, we explore the sensitivity of the fit to reducing the Balmer Break component.

Unfortunately, none of the fits are fully satisfying. As will be discussed more fully in §8, while the fit is acceptable in a  $\chi^2$  sense, the interpretation of the parameters are less straightforward. The best-fit model leads to rather extreme properties for both the stars (extremely high central stellar densities) and the AGN (extremely high EW H $\alpha$   $> 3000 \text{ \AA}$  measured relative to the AGN continuum), neither of which have been observed in any other galaxy or AGN. So we consider it likely that we are missing a critical physical ingredient or insight in our modeling. For context, the SDSS AGN EW(H $\alpha$ ) is  $\sim 200 - 300 \text{ \AA}$  (Stern & Laor 2012) and the EW distribution of broad-line AGN found with JWST at these redshifts is  $\sim 500 \pm 300 \text{ \AA}$  (Maiolino et al. 2024a), so the EW H $\alpha$  of A2744–45924 is already quite high (relative to the observed total continuum). We note that a key assumption the AGN modeling performed here is the powerlaw shape of the AGN continuum. If the AGN continuum has a different shape, or itself features a Balmer break (Inayoshi & Maiolino 2024), a massive stellar component would not be needed.

## 6. X-RAY EMISSION

It has become clear that little red dots, and perhaps broad-line selected AGN more generally at  $z > 4$ , are very X-ray weak compared with lower-redshift sources (Furtak et al. 2023b, 2024; Yue et al. 2024; Maiolino et al. 2024a). With UNCOVER, we get the benefit of 2.14 Ms of *Chandra* imaging (Cycle 23; ACIS-I; Proposal ID 23700107; PI: A. Bogdan) and the small boost

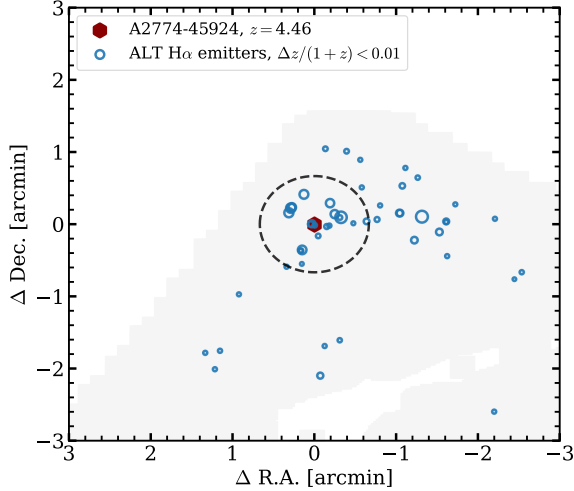


**Figure 7.** The overdensity around A2744–45924 as revealed by ALT spectroscopy. A2744–45924 is the red hexagon, and those of 40 galaxies with  $4.45 < z < 4.49$  as blue circles whose size correlates with their stellar mass. These were all identified via H $\alpha$  emission in ALT. For reference the circle represents 1 cMpc, while the grey region shows the ALT area with  $\mu < 3$ . There is a clear overdensity around A2744–45924 at this redshift.

of lensing ( $\mu = 1.7$ ). Our best constraint comes from the observed 2–7 keV, corresponding to a rest-frame 10–40 keV luminosity upper-limit of  $< 2 \times 10^{43}$  erg/s. At rest-frame 10–40 keV, hard X-ray photons are relatively insensitive to absorption up to and including extreme Compton-thick column densities of  $N_{\text{H}} \sim 10^{25} \text{ cm}^{-2}$ . Relative to a standard X-ray bolometric correction of 80–90 (Duras et al. 2020), A2744–45924 is nominally 10 times weaker in the X-rays than would be expected assuming the broad H $\alpha$  is photoionized by a normal UV-emitting AGN (see §8). Any reddening correction would only make A2744–45924 intrinsically weaker in the X-ray. Nominally, this level of X-ray weakness could be explained purely by absorption if  $N_{\text{H}} > 10^{25} \text{ cm}^{-2}$ . Although such a high value is quite extreme, the stellar and gas densities in these objects are also extreme. Alternatively, our limit is consistent with the higher end of the bolometric correction ( $L_{\text{X}}/L_{\text{bol}} = 100\text{--}1000$ ) that is derived for the most luminous quasars (e.g., Martocchia et al. 2017).

## 7. ENVIRONMENT

A2744–45924 is found in a large galaxy overdensity. We have already seen hints that some LRDs are preferentially associated with overdensities (Matthee et al. 2024a; Fujimoto et al. 2023a), but the extensive data in the Abell 2744 field enables the most comprehensive look at the environment of an LRD afforded to date.

With the ALT grism redshifts (Naidu et al. 2024), it is very clear that many galaxies are associated with this overdensity (Figure 7). There are 40 galaxies within  $\delta z = 0.02$  of A2744–45924 in the full  $27.5 \text{ arcmin}^2$  coverage in this redshift interval. A2744–45924 is about 50 arcsec away from the edge of the field of view of the ALT data. In the full  $z = 4 - 5$  coverage, ALT detects 17.6 galaxies per  $\Delta z = 0.04$  on average. This suggests that A2744–45924 is in a mild over-density of  $\delta = N/\langle N \rangle - 1 = 1.3$ . However, as seen in Fig. 7, most are at relatively small angular separations. Half are within 30 arcsec, with an over-density  $\delta \approx 40$ . This over-density is similar to some of the most UV luminous QSOs at  $z \sim 6 - 7$  (Eilers et al. 2024), although as a class the high number densities of little red dots argues that they cannot occupy the same massive halos as UV-selected QSOs (Pizzati et al. 2024).

The left panel of Figure 8 shows the near environment of A2744–45924, in which a total of four galaxies are detected in H $\alpha$  emission in the ALT data. None of the three neighbours shows evidence for AGN activity. These galaxies are all found with velocity differences within  $80 \text{ km s}^{-1}$ , roughly the precision of the grism redshifts (e.g. Torralba-Torregrosa et al. 2024). One companion is found at a distance of 0.7 arcsec to A2744–45924 and has a stellar mass  $M_* = 4 \times 10^7 M_{\odot}$ , a second is 1.5 arcsec away and has  $M_* = 5 \times 10^8 M_{\odot}$ , while the third at 2.3 arcsec has  $M_* = 10^9 M_{\odot}$ . The latter two are interacting with each other as indicated by diffuse emission. These systems are very likely all in the virial radius of the same halo (2.5 arcsec is the virial radius of a  $3 \times 10^{10} M_{\odot}$  halo at  $z = 4.5$ ; e.g. Behroozi et al. 2019) and bound to the same system.

We empirically compare the environment of A2744–45924 to the environments of other galaxies in the same dataset. Both as a comparison set and a tracer of the galaxy density we used other ALT galaxies with spectroscopically measured redshifts at  $z = 4 - 5$  with a magnification  $\mu < 3$  and  $L_{\text{H}\alpha} > 2 \times 10^{41} \text{ erg s}^{-1}$  (see Matthee et al. in prep for details). We count the number of neighbors with increasing distance (along the projected direction, in the source-plane modeled using the Furtak et al. 2023c magnification model), with a redshift difference of  $\Delta z/(1+z) < 0.01$  (i.e.  $3000 \text{ km s}^{-1}$ ). For the comparison set, we count the average number of neighbors around galaxies in a range of stellar masses. The rationale of this empirical comparison is that the galaxy and galaxy-pair selection functions are identical and that the completeness of these selections only mildly vary with redshift and across the field of view, especially with our luminosity cut. When calculating average neighbouring source density, we calculate

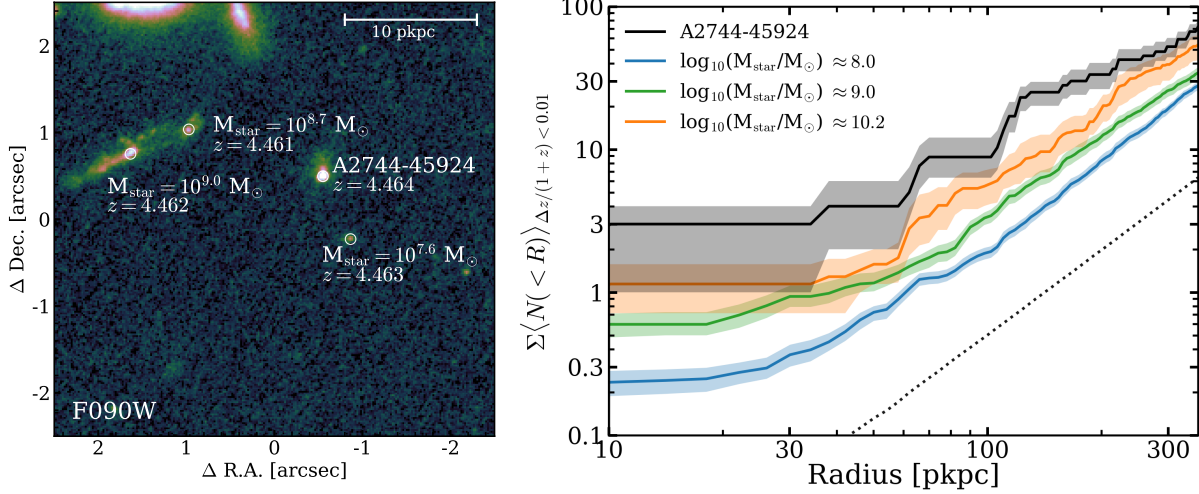


**Figure 8.** *Left:* The neighboring galaxies to A2744–45924 in the NIRCcam F090W image. We highlight the masses and redshifts of other galaxies for which ALT detected  $H\alpha$  emission. *Right:* The average number of neighbours within  $\Delta z/(1+z) < 0.01$  as a function of increasing projected radii in the source-plane around A2744–45924 and around normal star forming galaxies at  $z = 4$ – from the ALT survey for various stellar masses, compared to the random expectation. Errors are from bootstrapping the pairs (in the case of A2744–45924) or the central galaxies (in the stellar mass bins). The dashed line (normalised to the blue curve) shows the expectation around a random position.

the effective covered area taking the edges of the field of view and the masked  $\mu > 3$  regions into account.

Fig. 8 shows the measurement for A2744–45924 compared to the average neighbouring galaxy counts around 149, 62 and 7 sources with  $M_{\star} \approx 10^{8,9,10.2} M_{\odot}$  respectively. We estimate the errors in the neighbouring counts around A2744–45924 by bootstrapping the neighbours with replacement. We bootstrap the comparison set to also capture the variation from source to source among that set. We detect that galaxy overdensities are dependent on mass, and that on all scales the overdensity around A2744–45924 is comparable or even higher than the most massive, non-LRD galaxies in the reference sample. There is an apparent flattening in the galaxy pair counts that occurs at scales 50 pkpc ( $\sim 8$  arcsec) likely due to satellites within the same dark matter halo.

In summary, A2744–45924 is found in one of the most overdense regions in ALT at  $z = 4 - 5$ , and the most overdense on  $\sim 1 - 2$  cMpc scales. The overdensity exceeds that found around galaxies with  $M_{\star} \sim 10^{10} M_{\odot}$ , which in itself is higher than around galaxies with lower masses. While we will not attempt to quantify the stellar mass from this overdensity, the richness provides indirect evidence for a high stellar mass (Matthee et al. 2024b). At this point it remains unclear whether either the recent merger history (i.e. the relatively nearby environment) or the very large-scale environment is important in either forming or triggering the black holes powering the little red dots. A clustering analysis of a

larger sample that would allow us to control for BH activity would be very valuable to explore the diversity in their environments quantitatively.

## 8. AN EXTREME LITTLE RED DOT

A2744–45924 is an extreme system. It is one of the brightest and most luminous little red dots known, even over wider areas (Kokorev et al. 2024; Kocovski et al. 2024; Akins et al. 2024; Wang et al. 2024a).

The broad observed  $H\alpha$  line width  $\text{FWHM}(H\alpha) = 4500$  km/s and luminosity  $L_{H\alpha} = 10^{44}$  erg/s are among the highest observed in any LRD. Meanwhile, the source also exhibits one of the strongest Balmer breaks seen in any source at  $z > 4$  (see Weibel et al. 2024, for a compilation). Regardless of the source of the continuum, A2744–45924 has a very high  $H\alpha$  rest-frame EW ( $W_{H\alpha,0} \sim 800 \text{ \AA}$ ), but this means that any significant contribution from a stellar continuum would cause the intrinsic EW (relative to AGN continuum only) to be much higher (§5.2).

In the following subsection, we explore a range of possible origins both for the broad emission lines and the strong Balmer continuum to see if there is a way to reconcile the peculiar extreme properties of A2744–45924. As of now there is no physical picture that naturally explains the high number densities, the apparent Balmer break, the implied extraordinary stellar density, the remarkable  $H\alpha$  (width, flux, and EW), and the lack of commensurate X-ray (Yue et al. 2024) and mid-infrared emission (Williams et al. 2024; Akins et al. 2024).

### 8.1. Broad Fe II Emission: Unambiguous Evidence for the Broad-line Region

One of the novel aspects of our analysis here is the detection of broad Fe II multiples throughout the UV (Figure 4), optical, and near-infrared spectrum (see Figure 11). These Fe multiplets are commonly seen in AGN continuum (e.g., Wills et al. 1985) and are a tell-tale signature that we are seeing emission from the broad-line region although we cannot spectrally resolve the lines in the UV. They are thought to be strongest in sources accreted close to their Eddington limit (e.g., Boroson & Green 1992). A persistent question about little red dots has been the origin of the blue and faint UV continuum. In this one case, we have clear evidence that the emission lines arise from the broad-line region of an accreting black hole. In principle, this emission could arise from scattered light, as seen in some lower-redshift AGN (e.g., Glikman et al. 2023). However, we do not favor an explanation where a reddened AGN (with some unreddened scattered light) produces the entire spectrum, because the inflection point in the spectrum occurs right at 3600 Å, which is the energy required to ionize  $n = 2$  hydrogen. As shown by Setton et al. (2024), the ensemble of little red dot spectra in the *JWST* archive always show an inflection point at the same wavelength. This is inconsistent with a combination of reddened directly-transmitted AGN continuum with scattered light, which would produce inflections at different wavelengths depending on the dust law and fraction of scattered light.

In summary, the detection of Fe II in this spectrum strongly implies that the emission lines throughout the spectrum emerge from broad-line region conditions and are photoionized by an accreting massive black hole. We caution that other little red dot spectra have quite different spectral morphologies (e.g., the triply imaged source has very weak metal lines, Furtak et al. 2024), so we cannot necessarily draw more general conclusions about other objects yet.

### 8.2. Implications of a Pure Stellar Continuum

Regardless of the origin of the emission lines, our best-fit models in §5.2 strongly prefer a galaxy-dominated continuum at rest-frame  $> 0.4\mu\text{m}$ . A stellar-only picture for A2744–45924 would also explain the lack of X-ray detection (see also Yue et al. 2024), as well as the lack of a hot dust upturn in the mid-infrared seen in general in little red dots (Williams et al. 2024), and potentially the lack of variability (Kokubo & Harikane 2024).

In Figure 9, we contextualize the implied stellar density of A2744–45924 compared to other little red dots (Baggen et al. 2023, 2024; Ma et al. 2024), contemporary massive and passive galaxies (Carnall et al. 2023;

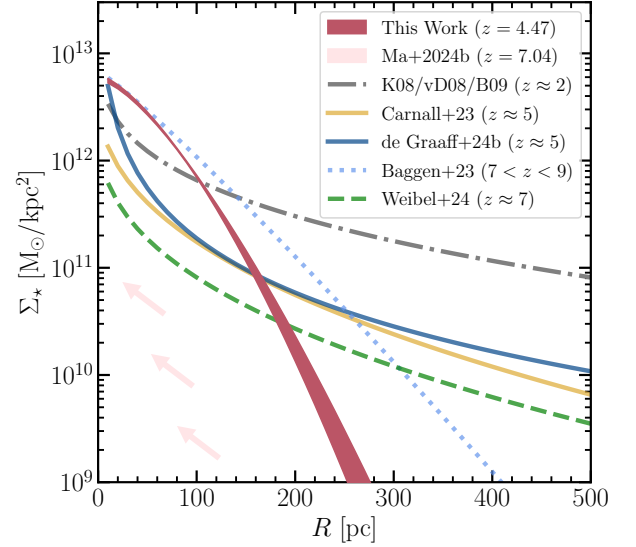


**Figure 9.** We compare the projected stellar density of A2744–45924 with *JWST*-detected objects at similar redshift from de Graaff et al. (2024c) and (Carnall et al. 2023), with higher-redshift little red dots from Baggen et al. (2023, see also Wang et al. 2024b), and  $z \sim 2.3$  compact red galaxies from Kriek et al. (2008, see also van Dokkum et al. 2008; Bezanson et al. 2009). In the stellar-only case, the density is high, but not much higher ( $\sim 2\times$ ), than an extrapolation of the cosmic noon sources.

de Graaff et al. 2024c), and lower-redshift massive and compact systems (Kriek et al. 2008; van Dokkum et al. 2008; Bezanson et al. 2009). These densities are high, but given the uncertainties they are not unprecedented (e.g., Norris et al. 2014). If we confirm the implied stellar densities, then it will have important implications for star formation at high density and the role of feedback (e.g., Hopkins et al. 2010; Grudić et al. 2019) and perhaps the role of dark matter in driving star formation (Boylan-Kolchin 2024).

Perhaps the hardest thing to explain about A2744–45924 in the absence of an AGN is the  $\text{H}\alpha$  luminosity. With an observed (magnification but not reddening-corrected)  $\text{H}\alpha$  luminosity of  $L_{\text{H}\alpha} = 10^{44}$  erg/s and a FWHM = 4500 km/s, this line is hard to explain given the observed continuum. The luminosity would require 500 – 1000  $M_{\odot}/\text{yr}$  of star formation to produce sufficient ionizing photons (Kennicutt & Evans 2012; Wilkins et al. 2019). Such a star-formation rate within a rest-frame optical size of  $< 70$  pc (see §3) would likely exceed the Eddington limit for star formation (e.g., Murray et al. 2005; Thompson et al. 2005; Hopkins et al. 2010). The faint UV fluxes imply that the star formation needs to be highly dust-reddened, further exacerbating the situation. The other possibility is that the broad  $\text{H}\alpha$  may be powered by supernovae (e.g., Terlevich &

Melnick 1985; Filippenko 1997). However, given that the number of ionizing photons from the supernovae is roughly 100 times lower than that from young stars at a fixed star formation rate (Johnson & Khochfar 2011), it seems very unlikely that supernovas could power this broad line (see also arguments in Maiolino et al. 2024a), unless the IMF is extremely top heavy.

### 8.3. Nature of the AGN

Taking the AGN presence as a given due to the presence of Fe II, we discuss the nature of the AGN. It is hard to avoid the conclusion that the AGN has properties that have not been observed in AGN before. First of all, the spectrum cannot be described by the combination of power-laws that constitute our current AGN models (§5.2). Furthermore, the broad-line EWs are quite high, and potentially much higher if stellar continuum dominates at 6564 Å. Finally, we observe that A2744–45924 is at least ten times fainter in the UV than expected from the H $\alpha$  line assuming typical type 1 QSOs (Vanden Berk et al. 2001), even with no reddening correction.

It is possible that the dearth of UV/optical and X-ray continuum from the AGN could be explained by a much higher covering factor of broad-line region clouds. The observed narrow associated Balmer absorption lines we see in A2744–45924 and other little red dots (20–30% Matthee et al. 2024a; Wang et al. 2024a; Kocevski et al. 2024; Juodžbalis et al. 2024) also may indicate an excess of high-density clouds. Only a small number of associated Balmer absorbers have been observed in lower-redshift broad-line quasars to date, almost exclusively in systems with known absorption systems in UV lines, known as Broad Absorption Line quasars (BALs; for an overview, see Hutchings et al. 2002; Schulze et al. 2018). The velocity distribution of the absorbers, falling within  $< 500$  km/s, strongly suggests that they sit at the outer part of the broad-line region, and the fact that there is sufficient hydrogen in an excited state to absorb H $\alpha$  requires densities  $n_e > 10^9$  cm $^{-3}$ . It is possible that these dense clouds are so numerous that they can mostly block the light from the physically smaller accretion disk, while still allowing broad-line region emission to escape (Kocevski et al. 2024; Maiolino et al. 2024a), as has been seen in the X-ray before (e.g., Ricci & Trakhtenbrot 2023). It is also possible that lower-metallicity gas can boost the observed EWs, since there are fewer metal lines available for cooling. This metallicity effect is seen in star-forming galaxies (e.g., Reddy et al. 2018). The presence of such dense clouds beyond the sublimation radius could also cause additional absorp-

tion even into the mid-infrared, leading to colder torus models (e.g., Williams et al. 2024; Wang et al. 2024a).

The other challenge in an AGN-dominated scenario is how to explain the strong Balmer break. In our current models, a relatively old stellar population is required to explain the observed break. We use the revised index from Wang et al. (2024b) to measure a strength of  $f_{\lambda 4100}/f_{\lambda 3670} = 2.4$  in A2744–45924. This Balmer break strength is higher than is reported by Wang et al. for similar compact red sources at  $z = 7 - 8$ . It is tempting to wonder whether the continuum could be coming from the accretion disk (Laor & Davis 2011) or the very dense gas in the broad-line region (e.g., Baldwin et al. 2004; Inayoshi & Maiolino 2024; Setton et al. 2024). However, this has yet to be observed in other AGN and more modeling work is needed to determine how and where such a continuum might form.

### 8.4. Implications for galaxy evolution and black hole growth

Little red dots are common, accounting for a few percent of the galaxy population at  $4 < z < 6$ . It is therefore important to consider the implications for galaxy and black hole growth under different possible interpretations of their SEDs. Granting that in our estimation the broad Balmer lines are likely powered by accretion onto a supermassive black hole, with some substantial contribution from an evolved stellar population, and granting that no scenario satisfactorily explains all of the observed phenomena, we muse about possible implications for the coevolution of black holes and galaxies.

The black hole to galaxy mass ratio appears to be quite high across the board in little red dots (e.g., Furtak et al. 2024; Kokorev et al. 2023). Given their high number density, a high ratio of  $M_{\text{BH}}/M_{\text{gal}}$  may have important implications for seeding mechanisms (e.g., Pacucci et al. 2023). However, we cannot be confident in either the black hole mass or the stellar mass.

The measured H $\alpha$  flux is  $f_{\text{H}\alpha} = 7.3 \times 10^{-16}$  erg/s/cm $^2$ /Å, corresponding to a magnification-corrected  $L_{\text{H}\alpha} \sim 10^{44}$  erg/s with no reddening correction. We thus infer a black hole mass of  $M_{\text{BH}} = 7 \times 10^8 M_{\odot}$  using the single-epoch scaling from Greene & Ho (2005). The dominant sources of error include the uncertain reddening correction (factors of several) and unusual spectral energy distribution precluding the unambiguous use of low-redshift scaling relations. Simply put, we do not know how to relate the observed H $\alpha$  luminosity to the radius of the broad-line region (e.g., Krolik 2001). We therefore consider the black hole mass an order of magnitude estimate at best. Our best fit host decomposition likewise yields  $M_* \sim 10^{11} M_{\odot}$ , con-

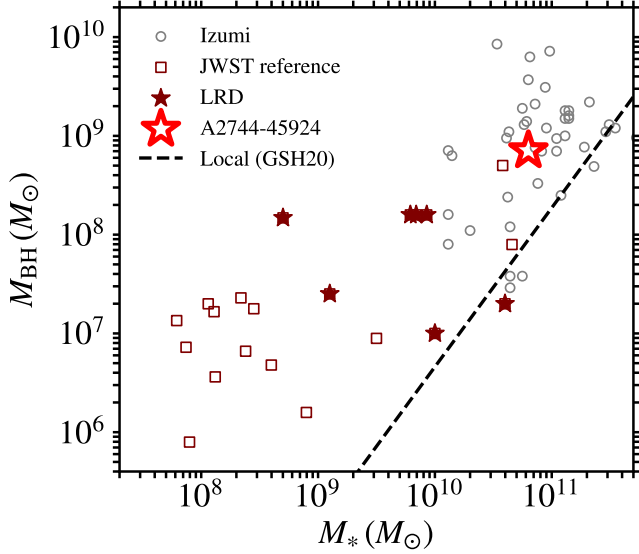


**Figure 10.** The position of A2744–45924 in a black hole mass–galaxy mass scaling relation plot. Since the inferred  $M_*$  is similar across Model II and III (and unconstrained in Model I), we simply show one value. In terms of  $M_{\text{BH}}$ , we note that the formal errors on all  $M_{\text{BH}}$  values are  $\sim 0.5$  dex (Shen 2013). However, in the case of little red dots, given the high  $\text{H}\alpha$  EWs and unknown bolometric (or UV) luminosities, we caution that the  $M_{\text{BH}}$  values are particularly systematics dominated. When taken at face value, A2744–45924 is not such a big outlier from the local scaling relations. For comparison, we show other broad-line samples, including little red dots from Fujimoto et al. (2022), Furtak et al. (2024), Kokorev et al. (2023), and Wang et al. (2024b) as filled stars, along with other AGN selections from Maiolino et al. (2023), Larson et al. (2023), and Chisholm et al. (2024) as open squares. The scaling relation line is taken from Greene et al. (2020).

sistent with the finding of significant clustering of nearby galaxies (Fig. 8). In that case, we find  $M_{\text{BH}}/M_{\text{gal}} \sim 1\%$  (Figure 10), which is certainly high compared to local relations (e.g., McConnell & Ma 2013) but not as dramatic of an outlier as other sources (Kokorev et al. 2023; Bogdán et al. 2024).

In this galaxy, many signs are pointing to very rapid assembly within an environment characterized by high gas density. Most of the red light in the source emerges from within  $r_e < 70$  pc, and we have argued above that the Balmer absorption requires very dense gas. Furthermore, the high-EW UV Nitrogen lines also seem to point to a rapid star formation event, although the presence of these lines has been used to argue for the presence of an AGN (Bunker et al. 2023; Übler et al. 2023; Maiolino et al. 2024b). Indeed, N III] is seen in stacks of narrow-line AGN (Hainline et al. 2011) and radio-selected narrow-line AGN (De Breuck et al. 2000).

On the other hand, these lines are only rarely seen in broad-line quasars (Bentz et al. 2004; Glikman et al. 2007; Jiang et al. 2008; Batra & Baldwin 2014). To date, a number of explanations for these Nitrogen lines have emerged that relate to the products of very massive stars, globular cluster formation (e.g., Senchyna et al. 2024), or even a tidal disruption event (e.g., Kochanek 2016). Regardless of the details, the current explanations of these lines all point to an event involving recent star formation (e.g., Cameron et al. 2023; Shi et al. 2024). The overdense environment and complicated UV morphology also are suggestive that some of the activity may be triggered by the environment.

## 9. SUMMARY

We present high SNR NIRSpec/PRISM, G395M grating, and NIRCам imaging for A2744–45924, one of the optically brightest little red dots known. Discovered from the UNCOVER survey (Bezanson et al. 2024), this object was photometrically identified (Labbé et al. 2023) and then observed for 16.3 hours with NIRSpec PRISM (Price et al. 2024).

A2744–45924 is unresolved in the rest-frame optical, with an upper limit to its size of  $r_e < 70 \pm 10$  pc. There is very blue  $n = 1$  asymmetric fluff detected in the rest-frame UV whose nature is yet unknown that is not included in the PRISM spectrum. From detailed modeling of the emission lines in the PRISM and grating spectra, we find clear evidence for a broad Fe II pseudo-continuum that argues strongly for an AGN to power the observed emission lines. Explaining the observed continuum proves more challenging. Our modeling strongly prefers that the rest-frame optical continuum be dominated by emission from a  $\sim 500$  Myr old stellar population with moderate reddening  $A_V \sim 1$ . The implied lower limit to the central stellar density of  $\sim 5 \times 10^{12} M_{\odot}/\text{kpc}^2$  appears as high as any observed stellar system. Furthermore, we have no mechanism to excite the  $L_{\text{H}\alpha} > 10^{44}$  erg/s broad emission line, except AGN activity. Other clues to the nature of the source include high-EW UV Nitrogen lines N III] and N IV], and narrow associated Balmer absorption of the broad  $\text{H}\alpha$  line. The implied rapid star-formation event that may have led to high Nitrogen enrichment may be related to the overdensity of galaxies found in the 100 kpc around A2744–45924.

This exploration of the properties of one luminous little red dot strongly suggests that AGN power at least some of these sources. To make more definitive progress on the composition of the host galaxy, high-resolution NIRSpec spectroscopy of the Balmer break region would provide qualitatively new information about the origin

of the continuum. Photometric monitoring, to search for variability, could provide another clue as to whether there is emission from accretion disk scales (e.g., Kokubo & Harikane 2024; Zhang et al. 2024). We will also observe this source with ALMA and MIRI, in an attempt to understand the bolometric luminosity and dust temperature (Setton in prep). These studies, hopefully combined with deep UV spectroscopy of a larger sample, may help us put together a more complete picture of this new and enigmatic class of objects.

#### ACKNOWLEDGMENTS

We acknowledge funding from JWST-GO-02561 and JWST-GO-04111, provided through a grant from the STScI under NASA contract NAS5-03127. I.L. acknowledges support from Australian Research Council Future Fellowship FT220100798. K.G. and T.N. acknowledge support from Australian Research Council Laureate Fellowship FL180100060. AZ acknowledges support by Grant No. 2020750 from the United States-Israel Binational Science Foundation (BSF) and Grant No. 2109066 from the United States National Science Foundation (NSF); by the Ministry of Science & Technology, Israel; and by the Israel Science Foundation Grant No. 864/23. JM and IK are funded by the European Union (ERC, AGENTS, 101076224). Views and opinions expressed are however those of the author(s) only and do not necessarily reflect those of the European Union or the European Research Council. Neither the European Union nor the granting authority can be held responsible for them. YF acknowledges supports from JSPS KAKENHI Grant Number JSPS KAKENHI Grant Numbers JP22K21349 and JP23K13149.

#### REFERENCES

- Abel, N. P., & Satyapal, S. 2008, *ApJ*, 678, 686, doi: [10.1086/529013](https://doi.org/10.1086/529013)
- Akins, H. B., Casey, C. M., Allen, N., et al. 2023, *ApJ*, 956, 61, doi: [10.3847/1538-4357/acef21](https://doi.org/10.3847/1538-4357/acef21)
- Akins, H. B., Casey, C. M., Lambrides, E., et al. 2024, arXiv e-prints, arXiv:2406.10341, doi: [10.48550/arXiv.2406.10341](https://doi.org/10.48550/arXiv.2406.10341)
- Alexandroff, R. M., Zakamska, N. L., Barth, A. J., et al. 2018, *MNRAS*, 479, 4936, doi: [10.1093/mnras/sty1685](https://doi.org/10.1093/mnras/sty1685)
- Atek, H., Labbé, I., Furtak, L. J., et al. 2024, *Nature*, 626, 975, doi: [10.1038/s41586-024-07043-6](https://doi.org/10.1038/s41586-024-07043-6)
- Baggen, J. F. W., van Dokkum, P., Labbé, I., et al. 2023, *ApJL*, 955, L12, doi: [10.3847/2041-8213/acf5ef](https://doi.org/10.3847/2041-8213/acf5ef)
- Baggen, J. F. W., van Dokkum, P., Brammer, G., et al. 2024, arXiv e-prints, arXiv:2408.07745, doi: [10.48550/arXiv.2408.07745](https://doi.org/10.48550/arXiv.2408.07745)
- Baldwin, J. A., Ferland, G. J., Korista, K. T., Hamann, F., & LaCluyzé, A. 2004, *ApJ*, 615, 610, doi: [10.1086/424683](https://doi.org/10.1086/424683)
- Banerji, M., Alaghband-Zadeh, S., Hewett, P. C., & McMahon, R. G. 2015, *MNRAS*, 447, 3368, doi: [10.1093/mnras/stu2649](https://doi.org/10.1093/mnras/stu2649)
- Barchiesi, L., Dessauges-Zavadsky, M., Vignali, C., et al. 2023, *A&A*, 675, A30, doi: [10.1051/0004-6361/202244838](https://doi.org/10.1051/0004-6361/202244838)
- Barro, G., Pérez-González, P. G., Kocevski, D. D., et al. 2024, *ApJ*, 963, 128, doi: [10.3847/1538-4357/ad167e](https://doi.org/10.3847/1538-4357/ad167e)
- Batra, N. D., & Baldwin, J. A. 2014, *MNRAS*, 439, 771, doi: [10.1093/mnras/stu007](https://doi.org/10.1093/mnras/stu007)

- Behroozi, P., Wechsler, R. H., Hearin, A. P., & Conroy, C. 2019, *MNRAS*, 488, 3143, doi: [10.1093/mnras/stz1182](https://doi.org/10.1093/mnras/stz1182)
- Bentz, M. C., Hall, P. B., & Osmer, P. S. 2004, *AJ*, 128, 561, doi: [10.1086/422346](https://doi.org/10.1086/422346)
- Berg, D. A., James, B. L., King, T., et al. 2022, *ApJS*, 261, 31, doi: [10.3847/1538-4365/ac6c03](https://doi.org/10.3847/1538-4365/ac6c03)
- Bezanson, R., van Dokkum, P. G., Tal, T., et al. 2009, *ApJ*, 697, 1290, doi: [10.1088/0004-637X/697/2/1290](https://doi.org/10.1088/0004-637X/697/2/1290)
- Bezanson, R., Labbe, I., Whitaker, K. E., et al. 2024, *ApJ*, 974, 92, doi: [10.3847/1538-4357/ad66cf](https://doi.org/10.3847/1538-4357/ad66cf)
- Bogdán, Á., Goulding, A. D., Natarajan, P., et al. 2024, *Nature Astronomy*, 8, 126, doi: [10.1038/s41550-023-02111-9](https://doi.org/10.1038/s41550-023-02111-9)
- Boroson, T. A., & Green, R. F. 1992, *ApJS*, 80, 109, doi: [10.1086/191661](https://doi.org/10.1086/191661)
- Boylan-Kolchin, M. 2024, arXiv e-prints, arXiv:2407.10900, doi: [10.48550/arXiv.2407.10900](https://doi.org/10.48550/arXiv.2407.10900)
- Brammer, G. 2022, msaexp: NIRSpec analysis tools, 0.3.4, Zenodo, Zenodo, doi: [10.5281/zenodo.7299500](https://doi.org/10.5281/zenodo.7299500)
- Buchner, J., Treister, E., Bauer, F. E., Sartori, L. F., & Schawinski, K. 2019, *ApJ*, 874, 117, doi: [10.3847/1538-4357/aafd32](https://doi.org/10.3847/1538-4357/aafd32)
- Bunker, A. J., Saxena, A., Cameron, A. J., et al. 2023, *A&A*, 677, A88, doi: [10.1051/0004-6361/202346159](https://doi.org/10.1051/0004-6361/202346159)
- Burgasser, A. J., Bezanson, R., Labbe, I., et al. 2024, *ApJ*, 962, 177, doi: [10.3847/1538-4357/ad206f](https://doi.org/10.3847/1538-4357/ad206f)
- Cameron, A. J., Katz, H., Rey, M. P., & Saxena, A. 2023, *MNRAS*, 523, 3516, doi: [10.1093/mnras/stad1579](https://doi.org/10.1093/mnras/stad1579)
- Carnall, A. C., McLure, R. J., Dunlop, J. S., et al. 2023, *Nature*, 619, 716, doi: [10.1038/s41586-023-06158-6](https://doi.org/10.1038/s41586-023-06158-6)
- Chabrier, G. 2003, *PASP*, 115, 763, doi: [10.1086/376392](https://doi.org/10.1086/376392)
- Chemerynska, I., Atek, H., Dayal, P., et al. 2024, arXiv e-prints, arXiv:2407.17110, doi: [10.48550/arXiv.2407.17110](https://doi.org/10.48550/arXiv.2407.17110)
- Chen, C.-H., Ho, L. C., Li, R., & Zhuang, M.-Y. 2024, arXiv e-prints, arXiv:2411.04446, doi: [10.48550/arXiv.2411.04446](https://doi.org/10.48550/arXiv.2411.04446)
- Chisholm, J., Berg, D. A., Endsley, R., et al. 2024, *MNRAS*, 534, 2633, doi: [10.1093/mnras/stae2199](https://doi.org/10.1093/mnras/stae2199)
- Conroy, C., & Gunn, J. E. 2010, *ApJ*, 712, 833, doi: [10.1088/0004-637X/712/2/833](https://doi.org/10.1088/0004-637X/712/2/833)
- Dayal, P. 2024, *A&A*, 690, A182, doi: [10.1051/0004-6361/202451481](https://doi.org/10.1051/0004-6361/202451481)
- De Breuck, C., Röttgering, H., Miley, G., van Breugel, W., & Best, P. 2000, *A&A*, 362, 519, doi: [10.48550/arXiv.astro-ph/0008264](https://doi.org/10.48550/arXiv.astro-ph/0008264)
- de Graaff, A., Brammer, G., Weibel, A., et al. 2024a, arXiv e-prints, arXiv:2409.05948, doi: [10.48550/arXiv.2409.05948](https://doi.org/10.48550/arXiv.2409.05948)
- de Graaff, A., Rix, H.-W., Carniani, S., et al. 2024b, *A&A*, 684, A87, doi: [10.1051/0004-6361/202347755](https://doi.org/10.1051/0004-6361/202347755)
- de Graaff, A., Setton, D. J., Brammer, G., et al. 2024c, arXiv e-prints, arXiv:2404.05683, doi: [10.48550/arXiv.2404.05683](https://doi.org/10.48550/arXiv.2404.05683)
- D'Eugenio, F., Cameron, A. J., Scholtz, J., et al. 2024, arXiv e-prints, arXiv:2404.06531, doi: [10.48550/arXiv.2404.06531](https://doi.org/10.48550/arXiv.2404.06531)
- Dong, X.-B., Wang, J.-G., Ho, L. C., et al. 2011, *ApJ*, 736, 86, doi: [10.1088/0004-637X/736/2/86](https://doi.org/10.1088/0004-637X/736/2/86)
- Duras, F., Bongiorno, A., Ricci, F., et al. 2020, *A&A*, 636, A73, doi: [10.1051/0004-6361/201936817](https://doi.org/10.1051/0004-6361/201936817)
- Eilers, A.-C., Mackenzie, R., Pizzati, E., et al. 2024, *ApJ*, 974, 275, doi: [10.3847/1538-4357/ad778b](https://doi.org/10.3847/1538-4357/ad778b)
- Fan, X., Bañados, E., & Simcoe, R. A. 2023, *ARA&A*, 61, 373, doi: [10.1146/annurev-astro-052920-102455](https://doi.org/10.1146/annurev-astro-052920-102455)
- Feroz, F., Hobson, M. P., & Trotta, R. 2010, arXiv e-prints, arXiv:1001.0719, doi: [10.48550/arXiv.1001.0719](https://doi.org/10.48550/arXiv.1001.0719)
- Ferruit, P., Jakobsen, P., Giardino, G., et al. 2022, *A&A*, 661, A81, doi: [10.1051/0004-6361/202142673](https://doi.org/10.1051/0004-6361/202142673)
- Filippenko, A. V. 1997, *ARA&A*, 35, 309, doi: [10.1146/annurev.astro.35.1.309](https://doi.org/10.1146/annurev.astro.35.1.309)
- Fosbury, R. A. E., Villar-Martín, M., Humphrey, A., et al. 2003, *ApJ*, 596, 797, doi: [10.1086/378228](https://doi.org/10.1086/378228)
- Fujimoto, S., Brammer, G. B., Watson, D., et al. 2022, *Nature*, 604, 261, doi: [10.1038/s41586-022-04454-1](https://doi.org/10.1038/s41586-022-04454-1)
- Fujimoto, S., Wang, B., Weaver, J., et al. 2023a, arXiv e-prints, arXiv:2308.11609, doi: [10.48550/arXiv.2308.11609](https://doi.org/10.48550/arXiv.2308.11609)
- Fujimoto, S., Kohno, K., Ouchi, M., et al. 2023b, arXiv e-prints, arXiv:2303.01658, doi: [10.48550/arXiv.2303.01658](https://doi.org/10.48550/arXiv.2303.01658)
- Furtak, L. J., Zitrin, A., Plat, A., et al. 2023a, *ApJ*, 952, 142, doi: [10.3847/1538-4357/acdc9d](https://doi.org/10.3847/1538-4357/acdc9d)
- . 2023b, *ApJ*, 952, 142, doi: [10.3847/1538-4357/acdc9d](https://doi.org/10.3847/1538-4357/acdc9d)
- Furtak, L. J., Zitrin, A., Weaver, J. R., et al. 2023c, *MNRAS*, 523, 4568, doi: [10.1093/mnras/stad1627](https://doi.org/10.1093/mnras/stad1627)
- Furtak, L. J., Labbé, I., Zitrin, A., et al. 2024, *Nature*, 628, 57, doi: [10.1038/s41586-024-07184-8](https://doi.org/10.1038/s41586-024-07184-8)
- Glikman, E., Djorgovski, S. G., Stern, D., Bogosavljević, M., & Mahabal, A. 2007, *ApJL*, 663, L73, doi: [10.1086/520085](https://doi.org/10.1086/520085)
- Glikman, E., Urrutia, T., Lacy, M., et al. 2012, *ApJ*, 757, 51, doi: [10.1088/0004-637X/757/1/51](https://doi.org/10.1088/0004-637X/757/1/51)
- Glikman, E., Rusu, C. E., Chen, G. C. F., et al. 2023, *ApJ*, 943, 25, doi: [10.3847/1538-4357/aca093](https://doi.org/10.3847/1538-4357/aca093)
- Goulding, A. D., Greene, J. E., Setton, D. J., et al. 2023, *ApJL*, 955, L24, doi: [10.3847/2041-8213/acf7c5](https://doi.org/10.3847/2041-8213/acf7c5)
- Greene, J. E., & Ho, L. C. 2005, *ApJ*, 630, 122, doi: [10.1086/431897](https://doi.org/10.1086/431897)

- Greene, J. E., Strader, J., & Ho, L. C. 2020, *ARA&A*, 58, 257, doi: [10.1146/annurev-astro-032620-021835](https://doi.org/10.1146/annurev-astro-032620-021835)
- Greene, J. E., Labbe, I., Goulding, A. D., et al. 2024, *ApJ*, 964, 39, doi: [10.3847/1538-4357/ad1e5f](https://doi.org/10.3847/1538-4357/ad1e5f)
- Groves, B. A., Heckman, T. M., & Kauffmann, G. 2006, *MNRAS*, 371, 1559, doi: [10.1111/j.1365-2966.2006.10812.x](https://doi.org/10.1111/j.1365-2966.2006.10812.x)
- Grudić, M. Y., Hopkins, P. F., Quataert, E., & Murray, N. 2019, *MNRAS*, 483, 5548, doi: [10.1093/mnras/sty3386](https://doi.org/10.1093/mnras/sty3386)
- Habouzit, M., Onoue, M., Bañados, E., et al. 2022, *MNRAS*, 511, 3751, doi: [10.1093/mnras/stac225](https://doi.org/10.1093/mnras/stac225)
- Hainline, K. N., Shapley, A. E., Greene, J. E., & Steidel, C. C. 2011, *ApJ*, 733, 31, doi: [10.1088/0004-637X/733/1/31](https://doi.org/10.1088/0004-637X/733/1/31)
- Harikane, Y., Ono, Y., Ouchi, M., et al. 2022, *ApJS*, 259, 20, doi: [10.3847/1538-4365/ac3dfc](https://doi.org/10.3847/1538-4365/ac3dfc)
- Hoffman, M., Sountsov, P., Dillon, J. V., et al. 2019, arXiv preprint arXiv:1903.03704
- Hoffman, M. D., Gelman, A., et al. 2014, *J. Mach. Learn. Res.*, 15, 1593
- Hopkins, P. F., Murray, N., Quataert, E., & Thompson, T. A. 2010, *MNRAS*, 401, L19, doi: [10.1111/j.1745-3933.2009.00777.x](https://doi.org/10.1111/j.1745-3933.2009.00777.x)
- Horne, K. 1986, *PASP*, 98, 609, doi: [10.1086/131801](https://doi.org/10.1086/131801)
- Humphrey, A., Villar-Martín, M., Vernet, J., et al. 2008, *MNRAS*, 383, 11, doi: [10.1111/j.1365-2966.2007.12506.x](https://doi.org/10.1111/j.1365-2966.2007.12506.x)
- Hutchings, J. B., Crenshaw, D. M., Kraemer, S. B., et al. 2002, *AJ*, 124, 2543, doi: [10.1086/344080](https://doi.org/10.1086/344080)
- Inayoshi, K., & Maiolino, R. 2024, arXiv e-prints, arXiv:2409.07805, doi: [10.48550/arXiv.2409.07805](https://doi.org/10.48550/arXiv.2409.07805)
- Isobe, Y., Ouchi, M., Tominaga, N., et al. 2023, *ApJ*, 959, 100, doi: [10.3847/1538-4357/ad09be](https://doi.org/10.3847/1538-4357/ad09be)
- Jakobsen, P., Ferruit, P., Alves de Oliveira, C., et al. 2022, *A&A*, 661, A80, doi: [10.1051/0004-6361/202142663](https://doi.org/10.1051/0004-6361/202142663)
- Jiang, L., Fan, X., & Vestergaard, M. 2008, *ApJ*, 679, 962, doi: [10.1086/587868](https://doi.org/10.1086/587868)
- Johnson, J. L., & Khochfar, S. 2011, *ApJ*, 743, 126, doi: [10.1088/0004-637X/743/2/126](https://doi.org/10.1088/0004-637X/743/2/126)
- Juodžbalis, I., Ji, X., Maiolino, R., et al. 2024, arXiv e-prints, arXiv:2407.08643, doi: [10.48550/arXiv.2407.08643](https://doi.org/10.48550/arXiv.2407.08643)
- Kashino, D., Lilly, S. J., Matthee, J., et al. 2023, *ApJ*, 950, 66, doi: [10.3847/1538-4357/acc588](https://doi.org/10.3847/1538-4357/acc588)
- Kennicutt, R. C., & Evans, N. J. 2012, *ARA&A*, 50, 531, doi: [10.1146/annurev-astro-081811-125610](https://doi.org/10.1146/annurev-astro-081811-125610)
- Killi, M., Watson, D., Brammer, G., et al. 2024, *A&A*, 691, A52, doi: [10.1051/0004-6361/202348857](https://doi.org/10.1051/0004-6361/202348857)
- Kocevski, D. D., Onoue, M., Inayoshi, K., et al. 2023, *ApJL*, 954, L4, doi: [10.3847/2041-8213/ace5a0](https://doi.org/10.3847/2041-8213/ace5a0)
- Kocevski, D. D., Finkelstein, S. L., Barro, G., et al. 2024, arXiv e-prints, arXiv:2404.03576, doi: [10.48550/arXiv.2404.03576](https://doi.org/10.48550/arXiv.2404.03576)
- Kochanek, C. S. 2016, *MNRAS*, 458, 127, doi: [10.1093/mnras/stw267](https://doi.org/10.1093/mnras/stw267)
- Kokorev, V., Fujimoto, S., Labbe, I., et al. 2023, *ApJL*, 957, L7, doi: [10.3847/2041-8213/ad037a](https://doi.org/10.3847/2041-8213/ad037a)
- Kokorev, V., Caputi, K. I., Greene, J. E., et al. 2024, *ApJ*, 968, 38, doi: [10.3847/1538-4357/ad4265](https://doi.org/10.3847/1538-4357/ad4265)
- Kokubo, M., & Harikane, Y. 2024, arXiv e-prints, arXiv:2407.04777, doi: [10.48550/arXiv.2407.04777](https://doi.org/10.48550/arXiv.2407.04777)
- Kovačević, J., Popović, L. Č., & Dimitrijević, M. S. 2010, *ApJS*, 189, 15, doi: [10.1088/0067-0049/189/1/15](https://doi.org/10.1088/0067-0049/189/1/15)
- Kraemer, S. B., & Crenshaw, D. M. 2000, *ApJ*, 532, 256, doi: [10.1086/308572](https://doi.org/10.1086/308572)
- Kriek, M., van Dokkum, P. G., Franx, M., et al. 2008, *ApJ*, 677, 219, doi: [10.1086/528945](https://doi.org/10.1086/528945)
- Krolik, J. H. 2001, *ApJ*, 551, 72, doi: [10.1086/320091](https://doi.org/10.1086/320091)
- Labbé, I., Greene, J. E., Bezanson, R., et al. 2023, arXiv e-prints, arXiv:2306.07320, doi: [10.48550/arXiv.2306.07320](https://doi.org/10.48550/arXiv.2306.07320)
- Langeroodi, D., & Hjorth, J. 2023, *ApJL*, 957, L27, doi: [10.3847/2041-8213/acfeec](https://doi.org/10.3847/2041-8213/acfeec)
- Laor, A., & Davis, S. W. 2011, *MNRAS*, 417, 681, doi: [10.1111/j.1365-2966.2011.19310.x](https://doi.org/10.1111/j.1365-2966.2011.19310.x)
- Larson, R. L., Finkelstein, S. L., Kocevski, D. D., et al. 2023, *ApJL*, 953, L29, doi: [10.3847/2041-8213/ace619](https://doi.org/10.3847/2041-8213/ace619)
- Le Fèvre, O., Lemaux, B. C., Nakajima, K., et al. 2019, *A&A*, 625, A51, doi: [10.1051/0004-6361/201732197](https://doi.org/10.1051/0004-6361/201732197)
- Leja, J., Carnall, A. C., Johnson, B. D., Conroy, C., & Speagle, J. S. 2019, *ApJ*, 876, 3, doi: [10.3847/1538-4357/ab133c](https://doi.org/10.3847/1538-4357/ab133c)
- Lotz, J. M., Koekemoer, A., Coe, D., et al. 2017, *ApJ*, 837, 97, doi: [10.3847/1538-4357/837/1/97](https://doi.org/10.3847/1538-4357/837/1/97)
- Ma, Y., Greene, J. E., Setton, D. J., et al. 2024, arXiv e-prints, arXiv:2410.06257, doi: [10.48550/arXiv.2410.06257](https://doi.org/10.48550/arXiv.2410.06257)
- Maiolino, R., Scholtz, J., Curtis-Lake, E., et al. 2023, arXiv e-prints, arXiv:2308.01230, doi: [10.48550/arXiv.2308.01230](https://doi.org/10.48550/arXiv.2308.01230)
- Maiolino, R., Risaliti, G., Signorini, M., et al. 2024a, arXiv e-prints, arXiv:2405.00504, doi: [10.48550/arXiv.2405.00504](https://doi.org/10.48550/arXiv.2405.00504)
- Maiolino, R., Scholtz, J., Witstok, J., et al. 2024b, *Nature*, 627, 59, doi: [10.1038/s41586-024-07052-5](https://doi.org/10.1038/s41586-024-07052-5)
- Marques-Chaves, R., Schaerer, D., Kuruvanthodi, A., et al. 2024, *A&A*, 681, A30, doi: [10.1051/0004-6361/202347411](https://doi.org/10.1051/0004-6361/202347411)
- Martocchia, S., Piconcelli, E., Zappacosta, L., et al. 2017, *A&A*, 608, A51, doi: [10.1051/0004-6361/201731314](https://doi.org/10.1051/0004-6361/201731314)

- Matthee, J., Naidu, R. P., Brammer, G., et al. 2024a, *ApJ*, 963, 129, doi: [10.3847/1538-4357/ad2345](https://doi.org/10.3847/1538-4357/ad2345)
- Matthee, J., Brammer, G., Weibel, A., et al. 2024b, *arXiv e-prints*, arXiv:2412.02846, doi: [10.48550/arXiv.2412.02846](https://doi.org/10.48550/arXiv.2412.02846)
- McConnell, N. J., & Ma, C.-P. 2013, *ApJ*, 764, 184, doi: [10.1088/0004-637X/764/2/184](https://doi.org/10.1088/0004-637X/764/2/184)
- Murray, N., Quataert, E., & Thompson, T. A. 2005, *ApJ*, 618, 569, doi: [10.1086/426067](https://doi.org/10.1086/426067)
- Naidu, R. P., Matthee, J., Kramarenko, I., et al. 2024, *arXiv e-prints*, arXiv:2410.01874, doi: [10.48550/arXiv.2410.01874](https://doi.org/10.48550/arXiv.2410.01874)
- Norris, M. A., Kannappan, S. J., Forbes, D. A., et al. 2014, *MNRAS*, 443, 1151, doi: [10.1093/mnras/stu1186](https://doi.org/10.1093/mnras/stu1186)
- Oke, J. B., & Gunn, J. E. 1983, *ApJ*, 266, 713, doi: [10.1086/160817](https://doi.org/10.1086/160817)
- Osterbrock, D. E. 1977, *ApJ*, 215, 733, doi: [10.1086/155407](https://doi.org/10.1086/155407)
- Pacucci, F., Nguyen, B., Carniani, S., Maiolino, R., & Fan, X. 2023, *ApJL*, 957, L3, doi: [10.3847/2041-8213/ad0158](https://doi.org/10.3847/2041-8213/ad0158)
- Pasha, I., & Miller, T. B. 2023, *The Journal of Open Source Software*, 8, 5703, doi: [10.21105/joss.05703](https://doi.org/10.21105/joss.05703)
- Pérez-González, P. G., Barro, G., Rieke, G. H., et al. 2024, *ApJ*, 968, 4, doi: [10.3847/1538-4357/ad38bb](https://doi.org/10.3847/1538-4357/ad38bb)
- Phan, D., Pradhan, N., & Jankowiak, M. 2019, *arXiv preprint arXiv:1912.11554*
- Pizzati, E., Hennawi, J. F., Schaye, J., et al. 2024, *arXiv e-prints*, arXiv:2409.18208, doi: [10.48550/arXiv.2409.18208](https://doi.org/10.48550/arXiv.2409.18208)
- Planck Collaboration, Aghanim, N., Akrami, Y., et al. 2020, *A&A*, 641, A6, doi: [10.1051/0004-6361/201833910](https://doi.org/10.1051/0004-6361/201833910)
- Price, S. H., Suess, K. A., Williams, C. C., et al. 2023, *arXiv e-prints*, arXiv:2310.02500, doi: [10.48550/arXiv.2310.02500](https://doi.org/10.48550/arXiv.2310.02500)
- Price, S. H., Bezanson, R., Labbe, I., et al. 2024, *arXiv e-prints*, arXiv:2408.03920, doi: [10.48550/arXiv.2408.03920](https://doi.org/10.48550/arXiv.2408.03920)
- Raiter, A., Fosbury, R. A. E., & Teimoorinia, H. 2010, *A&A*, 510, A109, doi: [10.1051/0004-6361/200912429](https://doi.org/10.1051/0004-6361/200912429)
- Reddy, N. A., Shapley, A. E., Sanders, R. L., et al. 2018, *ApJ*, 869, 92, doi: [10.3847/1538-4357/aaed1e](https://doi.org/10.3847/1538-4357/aaed1e)
- Ricci, C., & Trakhtenbrot, B. 2023, *Nature Astronomy*, 7, 1282, doi: [10.1038/s41550-023-02108-4](https://doi.org/10.1038/s41550-023-02108-4)
- Rodriguez, J., Varnière, P., Tagger, M., & Durouchoux, P. 2002, *A&A*, 387, 487, doi: [10.1051/0004-6361:20000524](https://doi.org/10.1051/0004-6361:20000524)
- Salviander, S., Shields, G. A., Gebhardt, K., & Bonning, E. W. 2006, *NewAR*, 50, 803, doi: [10.1016/j.newar.2006.06.018](https://doi.org/10.1016/j.newar.2006.06.018)
- Scholtz, J., Maiolino, R., D'Eugenio, F., et al. 2023, *arXiv e-prints*, arXiv:2311.18731, doi: [10.48550/arXiv.2311.18731](https://doi.org/10.48550/arXiv.2311.18731)
- Schulze, A., Misawa, T., Zuo, W., & Wu, X.-B. 2018, *ApJ*, 853, 167, doi: [10.3847/1538-4357/aaa7f0](https://doi.org/10.3847/1538-4357/aaa7f0)
- Senchyna, P., Plat, A., Stark, D. P., et al. 2024, *ApJ*, 966, 92, doi: [10.3847/1538-4357/ad235e](https://doi.org/10.3847/1538-4357/ad235e)
- Setton, D. J., Greene, J. E., de Graaff, A., et al. 2024, *arXiv e-prints*, arXiv:2411.03424, <https://arxiv.org/abs/2411.03424>
- Shen, Y. 2013, *Bulletin of the Astronomical Society of India*, 41, 61, doi: [10.48550/arXiv.1302.2643](https://doi.org/10.48550/arXiv.1302.2643)
- Shen, Y., Wu, J., Jiang, L., et al. 2019, *ApJ*, 873, 35, doi: [10.3847/1538-4357/ab03d9](https://doi.org/10.3847/1538-4357/ab03d9)
- Shi, Y., Kremer, K., & Hopkins, P. F. 2024, *A&A*, 691, A24, doi: [10.1051/0004-6361/202450964](https://doi.org/10.1051/0004-6361/202450964)
- Sobral, D., Matthee, J., Darvish, B., et al. 2018, *MNRAS*, 477, 2817, doi: [10.1093/mnras/sty782](https://doi.org/10.1093/mnras/sty782)
- Stern, J., & Laor, A. 2012, *MNRAS*, 423, 600, doi: [10.1111/j.1365-2966.2012.20901.x](https://doi.org/10.1111/j.1365-2966.2012.20901.x)
- Suess, K. A., Weaver, J. R., Price, S. H., et al. 2024, *arXiv e-prints*, arXiv:2404.13132, doi: [10.48550/arXiv.2404.13132](https://doi.org/10.48550/arXiv.2404.13132)
- Terlevich, R., & Melnick, J. 1985, *MNRAS*, 213, 841, doi: [10.1093/mnras/213.4.841](https://doi.org/10.1093/mnras/213.4.841)
- Thompson, T. A., Quataert, E., & Murray, N. 2005, *ApJ*, 630, 167, doi: [10.1086/431923](https://doi.org/10.1086/431923)
- Topping, M. W., Stark, D. P., Endsley, R., et al. 2024, *MNRAS*, 529, 4087, doi: [10.1093/mnras/stae800](https://doi.org/10.1093/mnras/stae800)
- Torralba-Torregrosa, A., Matthee, J., Naidu, R. P., et al. 2024, *A&A*, 689, A44, doi: [10.1051/0004-6361/202450318](https://doi.org/10.1051/0004-6361/202450318)
- Treiber, H., Greene, J., Weaver, J. R., et al. 2024, *arXiv e-prints*, arXiv:2409.12232, doi: [10.48550/arXiv.2409.12232](https://doi.org/10.48550/arXiv.2409.12232)
- Tsuzuki, Y., Kawara, K., Yoshii, Y., et al. 2006, *ApJ*, 650, 57, doi: [10.1086/506376](https://doi.org/10.1086/506376)
- Übler, H., Maiolino, R., Curtis-Lake, E., et al. 2023, *A&A*, 677, A145, doi: [10.1051/0004-6361/202346137](https://doi.org/10.1051/0004-6361/202346137)
- van Dokkum, P. G., Franx, M., Kriek, M., et al. 2008, *ApJL*, 677, L5, doi: [10.1086/587874](https://doi.org/10.1086/587874)
- van Dokkum, P. G., Nelson, E. J., Franx, M., et al. 2015, *ApJ*, 813, 23, doi: [10.1088/0004-637X/813/1/23](https://doi.org/10.1088/0004-637X/813/1/23)
- Vanden Berk, D. E., Richards, G. T., Bauer, A., et al. 2001, *AJ*, 122, 549, doi: [10.1086/321167](https://doi.org/10.1086/321167)
- Vehtari, A., Gelman, A., Simpson, D., Carpenter, B., & Bürkner, P.-C. 2021, *Bayesian analysis*, 16, 667
- Véron-Cetty, M. P., Joly, M., & Véron, P. 2004, *A&A*, 417, 515, doi: [10.1051/0004-6361:20035714](https://doi.org/10.1051/0004-6361:20035714)
- Vestergaard, M., & Wilkes, B. J. 2001, *ApJS*, 134, 1, doi: [10.1086/320357](https://doi.org/10.1086/320357)
- Wang, B., Fujimoto, S., Labbé, I., et al. 2023, *ApJL*, 957, L34, doi: [10.3847/2041-8213/acfe07](https://doi.org/10.3847/2041-8213/acfe07)

- Wang, B., de Graaff, A., Davies, R. L., et al. 2024a, arXiv e-prints, arXiv:2403.02304, doi: [10.48550/arXiv.2403.02304](https://doi.org/10.48550/arXiv.2403.02304)
- Wang, B., Leja, J., de Graaff, A., et al. 2024b, ApJL, 969, L13, doi: [10.3847/2041-8213/ad55f7](https://doi.org/10.3847/2041-8213/ad55f7)
- Wang, B., Leja, J., Labbé, I., et al. 2024c, ApJS, 270, 12, doi: [10.3847/1538-4365/ad0846](https://doi.org/10.3847/1538-4365/ad0846)
- Weaver, J. R., Cutler, S. E., Pan, R., et al. 2024, ApJS, 270, 7, doi: [10.3847/1538-4365/ad07e0](https://doi.org/10.3847/1538-4365/ad07e0)
- Weibel, A., de Graaff, A., Setton, D. J., et al. 2024, arXiv e-prints, arXiv:2409.03829, doi: [10.48550/arXiv.2409.03829](https://doi.org/10.48550/arXiv.2409.03829)
- Wilkins, S. M., Lovell, C. C., & Stanway, E. R. 2019, MNRAS, 490, 5359, doi: [10.1093/mnras/stz2894](https://doi.org/10.1093/mnras/stz2894)
- Williams, C. C., Alberts, S., Ji, Z., et al. 2024, ApJ, 968, 34, doi: [10.3847/1538-4357/ad3f17](https://doi.org/10.3847/1538-4357/ad3f17)
- Wills, B. J., Netzer, H., & Wills, D. 1985, ApJ, 288, 94, doi: [10.1086/162767](https://doi.org/10.1086/162767)
- Yue, M., Eilers, A.-C., Ananna, T. T., et al. 2024, ApJL, 974, L26, doi: [10.3847/2041-8213/ad7eba](https://doi.org/10.3847/2041-8213/ad7eba)
- Zakamska, N. L., Strauss, M. A., Krolik, J. H., et al. 2006, AJ, 132, 1496, doi: [10.1086/506986](https://doi.org/10.1086/506986)
- Zhang, Z., Jiang, L., Liu, W., & Ho, L. C. 2024, arXiv e-prints, arXiv:2411.02729, doi: [10.48550/arXiv.2411.02729](https://doi.org/10.48550/arXiv.2411.02729)

**Table 2.** UV Emission Line Fluxes

Line	Component	$\lambda_{obs}$ (Å)	Flux ( $10^{-19}$ erg s $^{-1}$ cm $^{-2}$ )	I/I(H $\beta$ )
N IV]	Broad	1488	64.9 $\pm$ 1.7	0.13
C IV	Broad	1549	60.2 $\pm$ 1.7	0.12
He II	Broad	1640	15.8 $\pm$ 2.4	0.03
O III]	Broad	1666	19.4 $\pm$ 2.3	0.04
N III]	Broad	1750	67.8 $\pm$ 2.4	0.13
Fe II	Broad	1786	21.2 $\pm$ 3.2	0.04
[Ne III]+Si II	Broad	1815	31.8 $\pm$ 3.1	0.06
Al III	Broad	1860	17.0 $\pm$ 3.0	0.03
Si III]	Broad	1888	1.6 $\pm$ 1.1	0.00
C III]	Broad	1909	146.3 $\pm$ 3.0	0.28

NOTE—Note that at shorter wavelengths than H $\beta$ , broad and narrow components can not be reliably distinguished at NIRSpect PRISM resolution. The Fluxes are corrected for magnification  $\mu = 1.7 \pm 0.2$ . Relative intensities are to the broad component of H $\beta$ .

## APPENDIX

**Table 3.** FeII measurements

Ion	$\lambda$ [Å]	Flux [ $10^{-19}$ erg/s/cm $^2$ ]	EW	I/I(H $\beta$ )
Fe II-UV	(2200-2600)	295.2	151.2	0.40
Fe II-UV	(2600-3050)	332.1	186.5	0.45
Fe II-UV	(2200-3050)	628.0	338.2	0.84
Fe II-opt	(4000-4800)	233.9	59.0	0.46
Fe II-opt	(5000-5500)	441.0	103.3	0.87
Fe II-opt	(4000-5500)	705.9	168.1	1.39
Fe II-NIR	(9100-9300)	34.3	9.0	0.07
Ion	$\lambda$ [Å]	Ratio		
Fe II-UV/Mg II	(2200-3050)	10.6		
Fe II-UV/Fe II-opt	(2200-3050)	0.9		

### A. OPTICAL-NIR PRISM LINE FITS

We follow the same procedure as in §4.2 to model rest-frame optical and near-infrared emission lines. The results are shown in Figure 11. In addition to clear evidence for broad Balmer and Paschen lines, the most notable features are evidence for broad He II  $\lambda$ 4686, O I  $\lambda$ 8446, and Fe II emission, all indicating emission originating from the Broad line region.

### B. SED FITS

Here we explore further how fit quality changes with varying contributions of the old stellar population. The main purpose is to inspect how sensitive fit quality the relative contribution of a Balmer break component. As a starting point we take the joint model III (AGN+Stars, see §5.2.3) best-fit solution for the evolved stellar component  $\log(M/M_{\odot}) = 10.9$ . Then we keep all parameters except stellar mass the same (e.g., age,  $\tau$ , and  $A_V$ ), and fix stellar mass to ( $\log(M/M_{\odot}) = 10.9, 10.7, 10.3$ ) while refitting for the AGN component. The results are shown in Figure 12. As the contribution of the Balmer break component is reduced, the fit quality becomes rapidly worse. This highlights

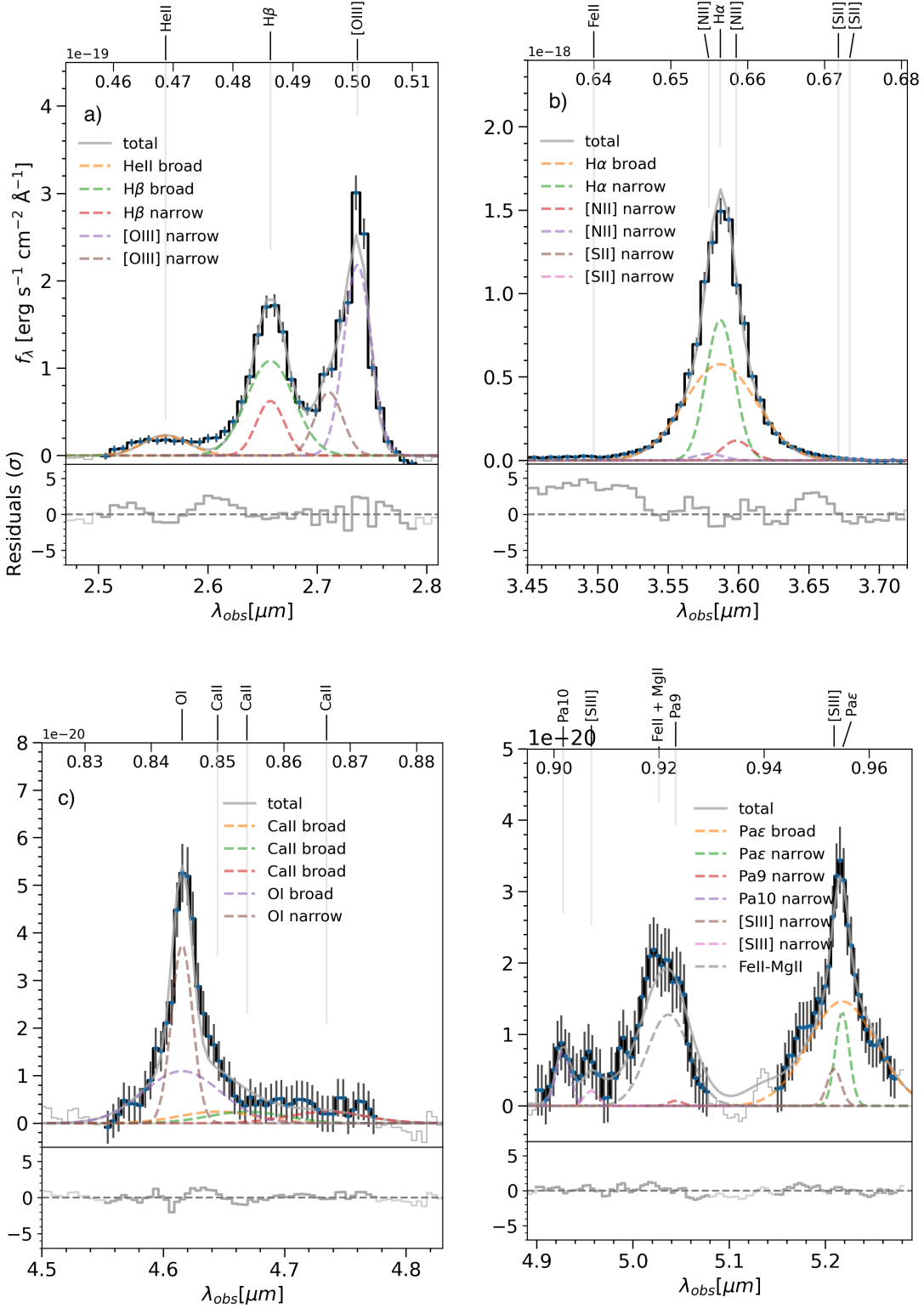


**Figure 11.** Model fits to the optical and near-IR lines. *Top panels:* optical emission lines: H $\beta$ , [O III] doublet, and He II  $\lambda 4686$  (a) and H $\alpha$ , N II doublet, S II doublet (b). Narrow and broad lines are indicated. A background was removed by subtracting a powerlaw fit to the continuum near the lines, and these areas were then masked (thin lines). Emission lines are modeled with Gaussians. Even at limited PRISM resolution a broad line component is required to model H $\alpha$  and H $\beta$ , while the O III doublet is well reproduced by an unresolved line alone, as is typically seen in broad line AGN. There is a clear evidence for excess flux blueward of H $\beta$ , likely a blend of broad He II  $\lambda 4686$  and optical Fe II emission (e.g., Fe II  $\lambda 4570$  Å bump). There is no evidence N II, S II emission, consistent with the higher-resolution NIRC2 GRISM data from ALT. There is a broad flux excess at  $\lambda\lambda 6200 - 6450$  Å, possibly indicating broad iron line emission Fe II  $\lambda 4570$  Å (Véron-Cetty et al. 2004). *Bottom panels:* NIR emission lines, showing O I, Ca II (Ca triplet, CaT) (c) Paschen-series, and S III (d). Pa $\epsilon$ , O I, and likely CaT have a broad component. Blueward of Pa9 there is a strong excess at  $9200$  Å, which we identify as the Fe II  $\lambda 9200$  Å bump. This emission is highly correlated with Fe II  $\lambda 4570$  Å in AGN, and its ratio can be used to constrain excitation mechanisms (?). Taken together, the optical-NIR line spectrum shows evidence for prominent broad line region emission lines.

**Table 4.** Balmer Line Series Fluxes

Line	Component	$\lambda_{obs}$ [Å]	Flux [ $10^{-19}$ erg s $^{-1}$ cm $^{-2}$ ]
H10	narrow	3799.014	$5.3 \pm 0.6$
H10	broad	3799.014	$11.7 \pm 1.2$
H9	broad	3836.511	$16.3 \pm 1.7$
H9	narrow	3836.511	$7.4 \pm 0.8$
H $\zeta$	narrow	3890.191	$10.8 \pm 1.2$
H $\zeta$	broad	3890.191	$23.9 \pm 2.5$
H $\epsilon$	broad	3971.236	$37.4 \pm 3.9$
H $\epsilon$	narrow	3971.236	$16.9 \pm 1.9$
H $\delta$	broad	4102.936	$64.1 \pm 6.7$
H $\delta$	narrow	4102.936	$28.9 \pm 3.2$
H $\gamma$	narrow	4341.731	$57.9 \pm 6.4$
H $\gamma$	broad	4341.731	$128.3 \pm 13.4$
H $\beta$	narrow	4862.738	$157.8 \pm 17.6$
H $\beta$	broad	4862.738	$349.9 \pm 36.6$
H $\alpha$	narrow	6564.697	$964.3 \pm 107.5$
H $\alpha$	broad	6564.697	$2137.8 \pm 123.4$

NOTE—Balmer Series fluxes for fiducial model III. These are the sum of the attenuated blue and red AGN Balmer series components. Note that at shorter wavelengths than  $H\beta$ , broad and narrow components can not be reliably distinguished at NIRSpect PRISM resolution. The Fluxes are corrected for magnification  $\mu = 1.7 \pm 0.2$ .

that a strong break at 3650 Å is difficult to produce with typical AGN models (based on a power-law continuum and emission lines). It is likely that the Balmer break component dominates the emission at rest-frame optical wavelengths.

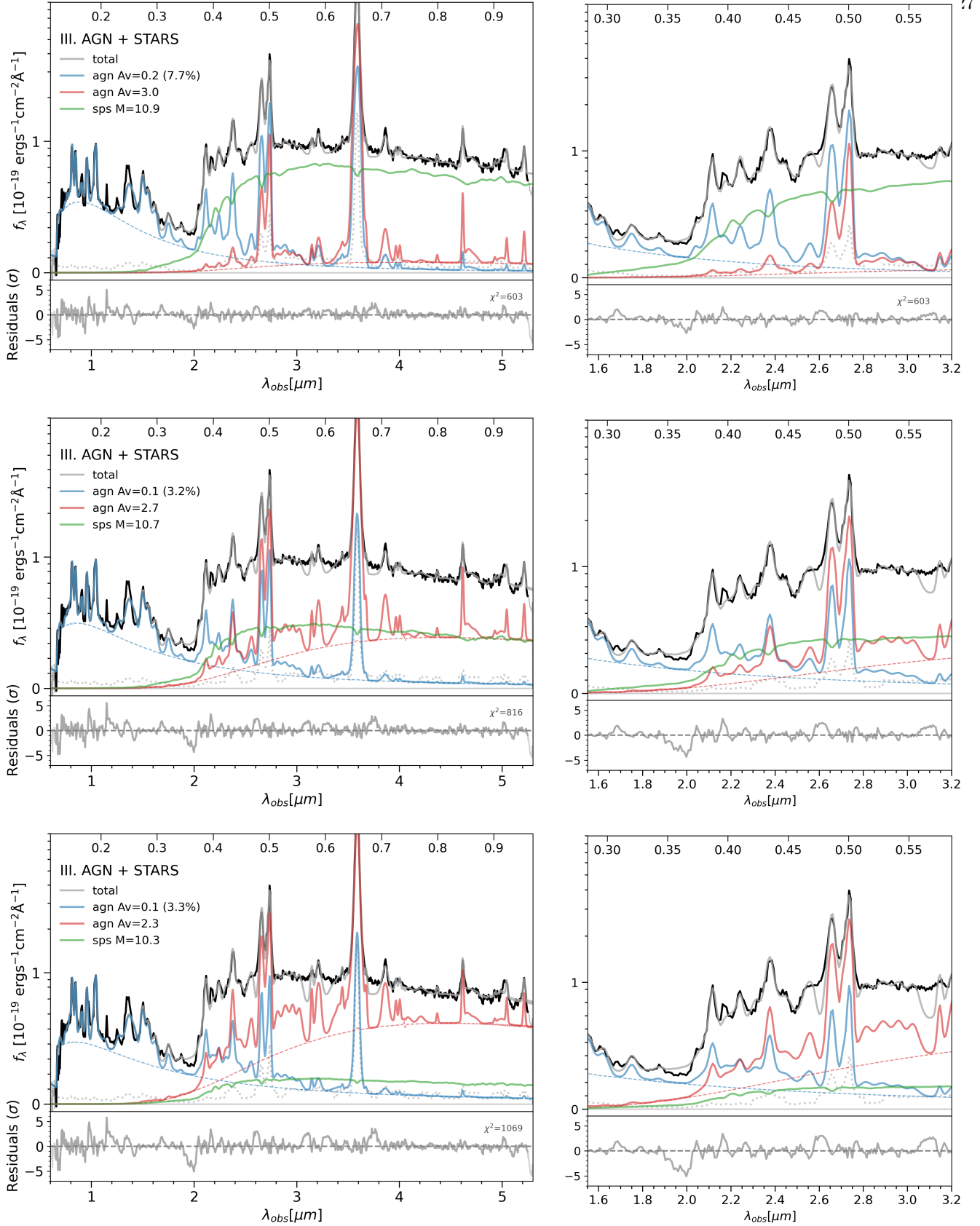


**Figure 12.** Model fits to the optical and near-IR lines, using the joint model III (AGN+Stars, see §5.2.3), but reducing the contribution of the evolved stellar population (*green*) in steps of 0.3 dex ( $\log(M/M_{\odot}) = 10.9, 10.6, 10.3$ ) and refitting. The fit residuals become significantly larger as soon as the contribution of the Balmer break component is reduced, especially in regions where Fe II is expected to be weak, which produces spurious absorption-like features. This highlights that a strong break at 3650 Å is difficult to produce with typical AGN models based on a power-law continuum and emission lines, and that the Balmer break component dominates the emission at rest-frame optical wavelengths.

**Table 5.** Other Emission Line Measurements

Ion	width	$\lambda$ [ Å ]	Flux [1e-19 erg/s/cm <sup>2</sup> ]	I/I(H $\beta$ )
Ly $\alpha$	narrow	1215.4	$4.1 \pm 0.4$	0.01
Mg II	broad	2799.1	$59.5 \pm 9.1$	0.08
He I	broad	3188.7	$5.1 \pm 2.2$	0.01
He II	broad	3204.0	$23.7 \pm 4.3$	0.03
[Ne V]	narrow	3426.8	$5.2 \pm 3.6$	0.01
[Ne V]	narrow	3426.8	$6.3 \pm 1.0$	0.01
[O II]	narrow	3727.1	$17.0 \pm 1.1$	0.02
[O II]	narrow	3729.9	$17.0 \pm 1.1$	0.02
[Ne III]	narrow	3869.9	$50.3 \pm 1.8$	0.07
He I	broad	3889.8	$13.1 \pm 4.9$	0.02
He I	broad	4027.3	$14.8 \pm 4.1$	0.02
[O III]	narrow	4364.4	$21.2 \pm 3.7$	0.03
He I	broad	4472.7	$23.5 \pm 4.0$	0.03
He II	broad	4685.7	$67.6 \pm 2.3$	0.09
[O III]	narrow	4960.3	$196.6 \pm 0.9$	0.26
[O III]	narrow	5008.2	$586.0 \pm 2.7$	0.79
[N II]	narrow	5756.2	$34.2 \pm 1.6$	0.05
He I	broad	5877.2	$110.0 \pm 3.8$	0.15
[O I]	narrow	6302.0	$11.5 \pm 1.8$	0.02
[N II]	narrow	6549.9	$82.3 \pm 36.4$	0.09
[N II]	narrow	6585.3	$246.8 \pm 109.2$	0.28
[S II]	narrow	6718.3	$19.1 \pm 1.5$	0.03
[S II]	narrow	6732.7	$19.1 \pm 1.5$	0.03
He I	broad	7067.1	$129.9 \pm 2.5$	0.17
O I	narrow	7256.4	$17.9 \pm 0.2$	0.02
[O II]	narrow	7321.9	$19.3 \pm 0.2$	0.03
[O II]	narrow	7332.2	$16.0 \pm 0.2$	0.02
O I	narrow	8446.7	$43.4 \pm 4.9$	0.08
O I	broad	8446.7	$57.0 \pm 10.8$	0.11
Ca II	broad	8500.4	$82.1 \pm 3.8$	0.11
Ca II	broad	8544.4	$82.1 \pm 3.8$	0.11
Ca II	broad	8664.5	$82.1 \pm 3.8$	0.11
Pa10	narrow	9017.4	$8.3 \pm 2.6$	0.02
[S III]	narrow	9071.1	$2.3 \pm 1.6$	0.00
Pa9	narrow	9231.6	$0.8 \pm 1.9$	0.00
[S III]	narrow	9533.2	$5.6 \pm 3.8$	0.01
Pa $\epsilon$	broad	9548.6	$76.0 \pm 6.4$	0.15
Pa $\epsilon$	narrow	9548.6	$14.1 \pm 4.1$	0.03

NOTE—Note that at rest-frame UV wavelengths, broad and narrow components cannot be reliably distinguished at NIRSpect PRISM resolution. The Fluxes are corrected for magnification  $\mu = 1.7 \pm 0.2$ . Relative intensities are to the broad component of H $\beta$ .

**Table 6.** Model configuration.

III. STARS + AGN				
Component	Parameter	Type	Value	Prior
all	dust_index	Free	(-1.8, -0.4)	Linear
all	z	Fixed	4.4655	—
all	lsf_scale	Fixed	1.3	—
agn_blue	broad_fwhm	Fixed	4850	—
agn_blue	narrow_fwhm	Fixed	650	—
agn_blue	Av	Free	(0.0, 1.0)	Linear
agn_blue	EW_Balmer_10kK_b	Free	(-1.0, 4.0)	Log <sub>10</sub>
agn_blue	EW_Balmer_10kK_n	Free	(-1.0, 4.0)	Log <sub>10</sub>
agn_blue	beta_1	Free	(-3.0, -1.0)	$N(-1.7, 0.3)$
agn_blue	L_beta_1	Free	(6.0, 15.0)	Log <sub>10</sub>
agn_red	Av	Free	(1.0, 5.0)	Linear
agn_red	L_beta_1	Free	(6.0, 15.0)	Log <sub>10</sub>
sps	lmass	Free	(7.0, 12.0)	Log <sub>10</sub>
sps	ltau	Free	(6.5, 9.0)	Log <sub>10</sub>
sps	lage	Free	(7.5, 9.2)	Log <sub>10</sub>
sps	logzsol	Free	(-1.0, 0.3)	Log <sub>10</sub>
sps	Av	Free	(0.0, 4.0)	Linear
sps	dust_type	Fixed	0	—
sps	sigma_smooth	Tied		0.5 * (Log <sub>10</sub> (M) - Log <sub>10</sub> (r <sub>e</sub> ) - 5.9)
sps	r_e	Fixed	0.07	—

NOTE—